nuclear fusion
IAEA

ACCEPTED MANUSCRIPT • OPEN ACCESS

Bolometer tomography on Wendelstein 7-X for study of radiation asymmetry

To cite this article before publication: Daihong Zhang *et al* 2021 *Nucl. Fusion* in press https://doi.org/10.1088/1741-4326/ac2778

Manuscript version: Accepted Manuscript

Accepted Manuscript is “the version of the article accepted for publication including all changes made as a result of the peer review process, and which may also include the addition to the article by IOP Publishing of a header, an article ID, a cover sheet and/or an ‘Accepted Manuscript’ watermark, but excluding any other editing, typesetting or other changes made by IOP Publishing and/or its licensors”

This Accepted Manuscript is **© 2021 The Author(s). Published by IOP Publishing Ltd.**.

As the Version of Record of this article is going to be / has been published on a gold open access basis under a CC BY 3.0 licence, this Accepted Manuscript is available for reuse under a CC BY 3.0 licence immediately.

Everyone is permitted to use all or part of the original content in this article, provided that they adhere to all the terms of the licence https://creativecommons.org/licences/by/3.0

Although reasonable endeavours have been taken to obtain all necessary permissions from third parties to include their copyrighted content within this article, their full citation and copyright line may not be present in this Accepted Manuscript version. Before using any content from this article, please refer to the Version of Record on IOPscience once published for full citation and copyright details, as permissions may be required. All third party content is fully copyright protected and is not published on a gold open access basis under a CC BY licence, unless that is specifically stated in the figure caption in the Version of Record.

View the article online for updates and enhancements.

This content was downloaded from IP address 192.188.106.22 on 27/09/2021 at 14:09

Bolometer tomography on Wendelstein 7-X for study of radiation asymmetry

D. Zhang, R. Burhenn, C.D. Beidler, Y. Feng, H. Thomsen, C. Brandt, S. Buller, F. Reimold, P. Hacker, R. Laube, J. Geiger, J. M. García Regaña[1], H. M. Smith, R. König, L. Giannone[2], F. Penzel[2], T. Klinger, J. Baldzuhn, S. Bozhenkov, T. Bräuer, J.K. Brunner, B. Buttenschön, H. Damm, M. Endler, F. Effenberg[3], G. Fuchert, Y. Gao, M. Jakubowski, J. Knauer, T. Kremeyer, M. Krychowiak, S. Kwak, H.P. Laqua, A. Langenberg, M. Otte, N. Pablant[3], E. Pasch, K. Rahbarnia, A. Pavone, L. Rudischhauser, J. Svensson, C. Killer, T. Windisch, and W7-X team*

Max-Planck-Institut für Plasmaphysik, D-17491 Greifswald, Germany
[1]Laboratorio Nacional de Fusión. CIEMAT, 28040 Madrid, Spain
[2]Max-Planck-Institut für Plasmaphysik, Garching, Germany
[3]Princeton Plasma Physics Laboratory, Princeton, NJ, USA
**T. Klinger et al., Nuclear Fusion 59 (2019) 112004 doi: 10.1088/1741-4326/ab03a7*

Abstract. The algorithm for bolometer tomography at Wendelstein 7-X (W7-X) has been recently improved using a novel regularization functional, based on relative gradient smoothing (RGS) of the sought radiation profile. It has been validated using radiation patterns provided by 3D modeling under real plasma conditions as phantoms and then applied to bolometer measurements performed during the first divertor operation phase of W7-X. The following results are presented: 1) edge-localized 2D radiation patterns with clearly resolved magnetic island radiation structures, 2) an up-down asymmetry in the impurity radiation that is not captured by the 3D edge plasma transport modeling, 3) reversal of the asymmetry with reversed magnetic field direction. Further analysis reveals a poloidal variation of the emissivity in the outer confined plasma region with a field-direction dependent asymmetry, also supported by the soft X-ray measurements. This asymmetry is considered to be related to asymmetric impurity distributions, driven by the pronounced ion-impurity friction force at the plasma edge where the collisionality of the W7-X plasma is sufficiently high to develop impurity asymmetry as predicted by neoclassical theory of parallel impurity transport.

1. Introduction

In magnetically confined plasma experiments, an accurate measurement of the radiation intensity distribution in the plasma is essential for power balance studies. The radiation profile provides information on the power loss due to impurity radiation and implicitly on impurity transport. The radiation profile evolution is essential for studying thermal instabilities that eventually lead to radiation collapse. In particular, a hollow emissivity profile is desirable as it implies low power loss and low impurity contamination in the core and simultaneously an intense cooling of the edge plasma, which is beneficial for plasma-facing components (PFCs). Usually, 2D (or even 3D) radiation profiles are necessary to describe the impurity radiation behavior since there are several physical mechanisms driving the asymmetric spatial distribution, in addition to spatially varying impurity sources. In earlier tokamak experiments, both low-Z and high-Z impurity asymmetries [1-4] have been observed in plasma regions far away from the impurity sources. Theoretical studies [5-9] conclude that friction forces between ions and impurity particles, centrifugal forces caused by plasma rotation, and poloidal variations of the electrostatic potential (enhanced by high-Z ions) are the leading mechanisms for the development of impurity asymmetry.

In stellarators/heliotron devices, the plasma does not rotate toroidally, but particles can be trapped in helical magnetic wells and escape from the plasma in the absence of collisions.

Therefore, special attention has been paid to the magnetic ripple-trapped particles [10]. Asymmetries in impurity radiation have also been observed experimentally [11-16] and in some cases are accompanied by thermal instability [12, 13]. The danger of impurity accumulation and the impact of electrostatic potential variation on impurity transport have also been considered [17-24].

Wendelstein 7-X (W7-X) [25] is an optimized stellarator, also regarding the reduction of neoclassical transport [26]. Its magnetic field topology is inherently 3D [27]. The divertor configurations utilize magnetic island chains that border the confined plasma region and the scrape off layer (SOL) shields the core plasma from direct penetration of impurities from the wall. Under the current wall conditions in W7-X these are usually low-Z elements, such as carbon and oxygen released from PFCs, e.g. the graphite targets. Predictive and interpretative numerical studies investigating the influence of edge impurity and neutral transport on the performance of the island divertor (such as power removal ability, compatibility between particle and power exhaust, and particle refueling capability of the recycling neutrals) in W7-X have been performed using the EMC3-EIRENE code [28, 29]. The beneficial effect of line emission due to low-Z impurities on ‘complete’ power removal from the plasma edge, i.e. plasma detachment, has been demonstrated in W7-X experiments [30, 31]. Questions about the actual distribution of the W7-X plasma radiation (e.g., what fraction of the radiated power is lost from the magnetic islands in the SOL and what fraction is lost within the confined plasma region) arise in light of the observations of the high power dissipation capability of the W7-X plasma, which is also predicted by 3D modeling [29].

On W7-X, plasma radiation is currently measured with a two-camera bolometer system [32]. It is designed to enable a tomographic reconstruction of the 2D radiation distributions in an up-down symmetric triangular plasma cross section. Nevertheless, the bolometer tomography faces challenges due to the limited number of lines of sight (LoS) in the present bolometer cameras, which have a sparse angular distribution (poloidally), and a large number of grid points adopted in the algorithm. The latter is imperative to achieve sufficient spatial resolution to resolve the complex radiation patterns expected in the periphery of the W7-X plasma.

Recently, a tomographic reconstruction algorithm [33] originally adopted from Ref. [34] and based on minimum Fisher regularization (MFR) has been improved by using a novel regularization functional. It is based on relative gradient smoothing (RGS) of the sought emission profiles. In combination with appropriately defined numerical grids and using additional anisotropic smoothing factors in radial and poloidal directions [35], this new algorithm is successfully validated using simulation results by 3D modeling as phantoms. It has been intensively applied to W7-X hydrogen discharges with electron cyclotron resonance heating (ECRH). Selected results are presented in this work in order to demonstrate its success in assessing impurity radiation asymmetry.

The paper is arranged as follows. Section 2 describes the experimental conditions, the bolometer system, and its general observation about W7-X plasma radiation asymmetry. Section 3 presents the algorithm for bolometer tomography. Section 4 shows the experimental and the analysis results. Section 5 addresses theoretical considerations and discussions. Section 6 concludes the paper.

2. Experimental conditions and the bolometer diagnostic at W7-X

2.1 Magnetic configuration and boundary condition

W7-X (major radius R = 5.5m; minor radius a ~0.5 m) is a modular stellarator of the HELIAS (Helical-Axis Advanced Stellarator) type with 5-fold symmetry. The magnetic field is generated by external non-planar (50) and planar (20) superconducting coils. The magnetic configuration is not axisymetric, so the poloidal cross section varies with the toroidal angle [27]. The magnetic configuration in the experiments studied here is the $\iota/2\pi = 5/5$ standard island divertor configuration (denoted SDC), in which five topologically independent helical island chains in the SOL helically enclose the core confinement region. Five pairs of carbon divertor units (at present without active water cooling) are installed periodically in the toroidal direction maintaining stellarator up-down symmetry, serving as particle and heat sinks. These are shown in Figure 1.

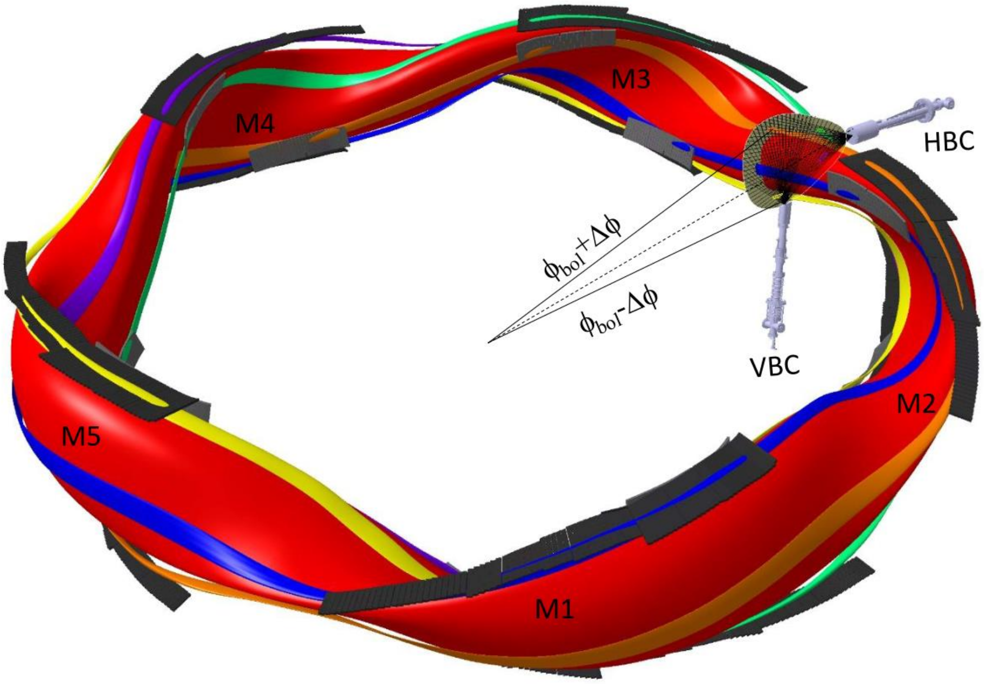

Figure 1. View of the stellarator W7-X in the ‘standard’ configuration (SDC) and the five pairs of symmetrically installed graphite divertor units (module M1-M5). The color bands indicate the five separate magnetic islands in the SOL. The location of the bolometer cameras (HBC and VBC) installed around a triangular cross-section (ϕ_{bol} = 108°) is shown, and a toroidal extension of the LoS in the VBC spanning from 105° to 111° is depicted with $\Delta\phi$=3°.

The impurities released by PFCs are mainly carbon and oxygen. In the plasma studied here (the so-called OP1.2a conducted in the year 2017), wall-boronisation has not yet been performed. As a consequnce, oxygen impurities could be additionally released by out-gassing, and normally plays a predominant role in its contribution to the total radiated power from the plasma [30]. This work is on hydrogen plasmas generated by ECRH in the X2-mode with an average magnetic field strength on the plasma axis B(0) = 2.5 T [36]. The normal magnetic field direction is counter-clockwise when viewing W7-X from the top.

2.2 The bolometer diagnostic

Line of sight geometry. The currently employed bolometer system on W7-X consists of two pinhole cameras [32]. They are installed around one of the five triangular cross sections (ϕ_{bol} = 108°) at W7-X (see Figure 1), which have an up-down symmetric magnetic topology as shown in Figure 2. The horizontal bolometer camera (HBC) has 32 main channels (and 32 secondary channels that are either covered with a Be-foil or use a non-blackened detector to obtain more information about the impurity radiation) viewing the plasma horizontally from the outboard side through a slit aperture. The LoS distribution is also constructed with up-down symmetry so that up-down symmetry of the plasma can be directly monitored. The vertical bolometer camera (VBC) consists of two separate detector arrays, located on the right and left when viewing the plasma from the bottom of W7-X, each with 24 channels (designated VBCr and VBCl). Only 9 channels in the VBCl are used for tomographic purposes, as the remaining channels have a field of view overlapping that of the VBCr. Here the LoS plane is aligned with the port geometry (with tilted port axis) due to limited space, and consequently extends toroidally over several degrees ($\phi = \phi_{\mathrm{bol}} \pm \Delta\phi$ with $\Delta\phi = 3°$). The LoS are fan-shaped, collimated by slit-apertures, each with a poloidal dimension of 0.5 cm and a toroidal dimension of 1.0 cm, and the etendue (see Eq. (2)) for the HBC is $\sim 1.4\times10^{-5}$ cm^2/sr and for VBCr and VBCl $\sim 6.2\times10^{-5}$ cm^2/sr.

The following aspects were considered while adjusting the camera geometry to ensure that as much information as possible could be acquired for tomographic reconstruction:

- ensure complete coverage over the entire plasma cross section under study, including both the confined and SOL plasma,
- minimize gaps (information loss) between two adjacent LoS (gap << LoS-width),
- maximize the common fields of view of the HBC and VBC.

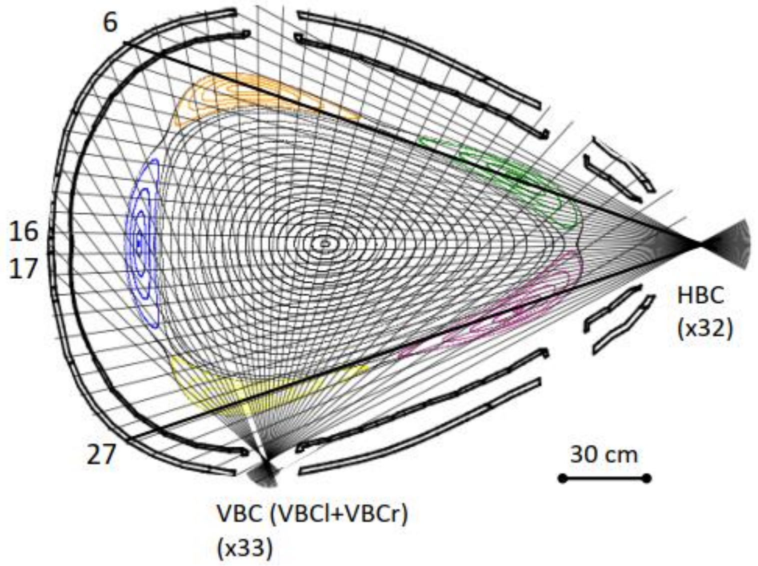

Figure 2. The LoS distribution of the HBC (32 channels) and VBC (24 channels in VBCr; 9 out of 24 channels in VBCl) around the triangular plasma cross section (ϕ = 108°) at W7-X, which has an up-down symmetric magnetic topology as shown by the Poincaré plots for the SDC. Two thick black lines show the LoS of ch6 and ch27 viewing the LCFS in the upper and lower half-planes, respectively. Two central channels (ch16 and ch17) with LoS through the plasma center are labeled accordingly. The five independent magnetic islands in the SOL are shown in colors.

Regarding the last point, the HBC is adjusted by rotation around the port axis (through ϕ_{bol}=108°) and its LoS plane is aligned with that of the VBC. Nevertheless, the system's center remains at ϕ_{bol}, and the HBC retains its ability to monitor the up-down symmetry of the plasma because the magnetic flux around the triangular cross section ($\phi = \phi_{\mathrm{bol}}$) satisfies stellarator symmetry (magnetic flux $\varphi\,[R, Z, \phi_{bol} + \Delta\phi] = \varphi\,[R, -Z, \phi_{bol} - \Delta\phi]$ where R is the major radius and Z is the vertical coordinate with Z=0 representing the plasma mid-plane). The whole LoS distribution of the system together with the Poincaré plot of the SDC configuration at ϕ_{bol} is shown in Figure 2. The spatial resolution, defined by the averaged LoS beam width in the plasma center is ~4 cm. In the SOL, the width of the LoS beam varies from 1.5 cm to 6.5 cm, which is much smaller than the poloidal island dimension of ~50 cm but close to the radial island dimension of ~7.0 cm. This means that the W7-X bolometer system, which is dedicated to resolving the 2D radiation distribution in the entire plasma cross-section, has a relatively poor radial resolution for the narrow SOL plasma, while having a reasonably good poloidal resolution.

It is noteworthy that no divertor target elements fall within the field of view of the bolometers, hence impacts of intense infrared (IR) radiation and energetic particles from the hot divertor targets on the measurements can be excluded.

Bolometer measurements. The detectors used for the W7-X bolometers are of the metal-resistive type [37] with a 5 μm thick gold absorber that has dimensions of 1.3 mm and 3.8 mm in the poloidal and toroidal directions, respectively. They are deposited on the front side of a ceramic (silicon nitride Si3N4) substrate, while the sensor and the reference resistor pair (both made of Pt) forming a Wheatstone bridge are located on the back side. A thin carbon layer (50 nm thick) has been sputtered onto the absorber to improve the detection efficiency for low-energy photons. A significant reduction in the reflectivity of visible light (by a factor of more than 5) has been confirmed in the laboratory by comparing the detection efficiency with that of the non-blackened detectors [38, 39]. The detectors are particularly sensitive to impurity line radiation, whose spectrum is mainly in the VUV and soft X-ray range (300 nm to 0.2 nm). Both the substrate and the Pt resistors are radiation resistant, and the overall design is a prototype for the ITER bolometer detectors under development [40]. The production variations between the sensor and the reference resistors are <2%, providing low offsets of the bolometer bridge, which is important to reduce the effects of thermal offset drift on signal accuracy [41], especially for long-pulse, high-power discharges.

The plasma radiated power *P* incident on the detector is calculated using the following equation

$$P = \frac{1}{f_t * s}\left[\tau \frac{du_d}{dt} + f_c * u_d\right], \tag{1}$$

where u_d is the bridge voltage signal, s is the detector sensitivity, and τ is its cooling-time coefficient (typically 0.1 s). These parameters are routinely calibrated before each discharge using an in-situ ohmic heating process [42]. f_c is a correction factor (~0.98) due to the resistance of the cables (40 m long) connecting the detectors in the machine vacuum and the electronics in the torus hall. f_t is the optical transmittance of the metal grids (~0.53) used for microwave shielding, which was a critical issue in the W7-X bolometer design because the metal foil absorber is also sensitive to scattered microwaves not absorbed by the plasma (microwave stray radiation). Despite the low absorption coefficient of 0.1%-1% (depending on surface roughness and oxidation), multipath microwave reflection within the detector housing can markedly increase the effective power flux impinging on the detectors. Successful suppression of the microwave impact to a negligible level (by a factor of ~300) is the prerequisite for accurate measurements by the W7-X bolometer system. Technical details can be found in Ref. [32, 43]. The value of f_t varies slightly for different detectors due to LoS geometry.

The errors in the bolometer measurements result mainly from the errors in the detector parameters and the noise level of the voltage signal u_d. Typically, the relative errors in both s and τ are ~1.5%. The latter is also sensitive to ambient neutral pressure in the range of $p_0>10^{-5}$ mbar (e.g., near the divertor chamber). The W7-X bolometer system is in a position having low p_0 ($\leq 10^{-6}$ mbar), as no neutral compression is to be expected here, thus ensuring stable operation. The noise level in u_d depends on the sampling period of the electronic system. Typically, a sampling period of 0.8 ms or 1.6 ms is used, which is a compromise between time resolution and signal-to-noise (S/N) ratio, and the corresponding noise level in u_d is ~ 2-5 μV (a noise equivalent power NEP ~1 μW). The S/N ratio for central bolometer channels is typically in the range of ten to hundreds.

2.3. General observations

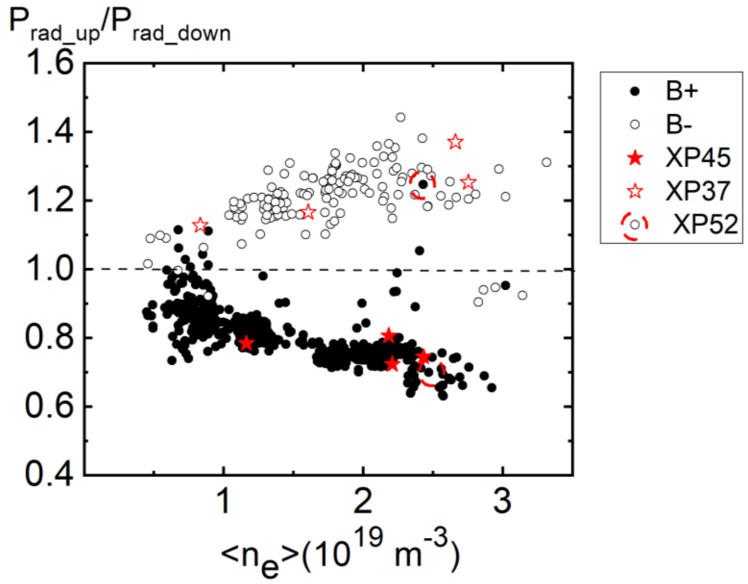

Figure 3. Density dependence of the ratio $f_{ud} = P_{rad\_up}/P_{rad\_down}$ in the SDC discharges during OP1.2a with normal (B+) and reversed (B-) magnetic field direction, which displays the asymmetry in plasma radiation. The data points marked with "star" are chosen for tomographic reconstructions.

During the first divertor operation phase of W7-X, experiments in the "standard" configuration have been performed in both the normal and reversed magnetic field direction (denoted here SDC+ and SDC-, respectively). The HBC has usually measured asymmetric chord brightness profiles, indicating different radiated power from up and down plasma regions (noted as $P_{rad,up}$ and $P_{rad,down}$, respectively) in the HBC viewed volume. Evaluations of $P_{rad,up}$ and $P_{rad,down}$ have been performed using the volume-weighted summation of the HBC measurements from the channels viewing the upper (channels 1-16) and the lower (channels 17-32) plasma regions, respectively (see Figure 2), which is similar to the calculations of the total plasma radiated power $P_{rad} = V_p \frac{\sum_1^{n_l} \bar{\varepsilon}_l V_l}{\sum_1^{n_l} V_l}$, where measurements of all channels of the HBC (channels 1-32) are taken into account (see Figure 8). Here, $\bar{\varepsilon}_l$ and V_l are the line-averaged emissivity and the viewing volume of channel l, and Vp is an effective plasma volume (both V_l and V_p are associated with the plasma region considered in Figure 4(b)). The ratio $f_{ud} = P_{rad,up}/P_{rad,down}$ quantifies the degree of up-down asymmetry and is shown for the quasi-steady-state plasmas (with P_{ECRH} from 2 MW to 5 MW) in Figure 3 as a function of plasma density. It is found that a) the data points fall into two branches with $f_{ud} > 1$ for most SDC- discharges and with $f_{ud} < 1$ for most SDC+ discharges, indicating the reversal of asymmetry after reversing the magnetic field direction, b) the degree of the asymmetry generally increases with line-averaged plasma density $<n_e>$, c) a similar trend for varied P_{ECRH}. Note that for similar $<n_e>$ and fixed P_{ECRH} the asymmetry can be different (see the two filled stars at $<n_e> = 2.2\times10^{19}$ m^{-3} that will be analyzed in a later section), indicating the role of local plasma parameters in influencing the radiation asymmetry. There are also special cases showing a turnover of the asymmetry during a discharge that occurs when the plasma shrinks (marked by dashed circles for XP20171109.52 labeled XP52), which is however not the focus of this work.

The observed asymmetry based on the HBC line-integrated measurements is robust for both magnetic field directions. And the search for the mechanism driving the asymmetry requires details of the radiation distribution using bolometer tomography.

3. The bolometer tomography and its performance

The goal of bolometer tomography is to reveal the spatial distribution of plasma emissivity ε (power per volume) using a series of line-integrated measurements:

$$P_l = \int \varepsilon \left[\frac{\cos(\alpha)\cos(\beta)A_D A_s}{4\pi d^2}\right] ds, \qquad l = 1, \dots, n_l - 1 \tag{2}$$

where P_l is the power measured by the detector numbered l and ds is a line element along the LoS. n_l is the total number of available signals. The quantity in the bracket is the etendue (see section 2.2), defined as the product of the effective detector area $A_D\cos(\alpha)$ and the observing solid angle $\Omega = \frac{\cos(\beta)A_s}{4\pi d^2}$, where $A_D = 4.9\times10^{-2}$ cm^2 and $A_s = 0.5$ cm^2 are the areas of the detector and aperture, respectively, α and β are the angles between the LoS and the normal of the detector and aperture, respectively, and d is the distance from the detector to the aperture. We assume here that the background plasma is optically thin.

These equations can be converted into linear equations by dividing the plasma cross-section into pixels:

$$P_l = \sum_{i=1}^{n_p} T_{li}\varepsilon_i\,, \tag{3}$$

where n_p is the number of pixels and T_{li} is the element of the geometric matrix T that fully describes the contribution of the emission ε_i from i-th pixel onto the l-th channel signal P_l. The tomography problem is thereby converted to finding the values ε_i in Eq. (3).

3.1 The approaches in the W7-X bolometer tomography

Grid definition and geometric matrix. Rectangular grids, commonly used in SXR tomography [34, 44], have proven to be unsuitable for W7-X bolometer tomography due to the limited number of available measurements ($n_l = 65$) and the large number of pixels ($n_p > 2000$) required for sufficient spatial resolution. Instead, the pixel grids are generated on cylindrical coordinates [R, ϕ, Z], where R is the major radius, ϕ is the toroidal angle, and Z is the height from the plasma mid-plane. The pixels formed on each ϕ-plane are fan-shaped and radially concentric around the plasma axis (see Figure 4 (b)) [45, 46]. In the confined plasma region, they are defined by the geometry of the closed magnetic flux surface (FS), which are taken from the VMEC equilibrium [27] as a reference. For the plasma studied here, which has a low plasma beta ($<\beta> < 0.5\%$) and therefore the plasma beta effects are small (W7-X was optimized for small beta effects on the equilibrium), the VMEC calculation of the magnetic vacuum configuration is used. The grids outside the last closed flux surface (LCFS) in the SOL are obtained by linear extrapolation of the magnetic structure near the LCFS. The grid points are specified in the magnetic coordinate system (r, θ, ϕ) due to the finite toroidal extent ($\Delta\phi \sim 3°$) (see Figure 1) of the LoS, where r is the effective radius of the closed or extended FS, θ is the poloidal angle with $\theta = 0$ at the outboard mid-plane, and θ increases in the counterclockwise direction (see Figure 4(b)). 3D pixels (i.e., voxels) are thereby created along the flux tubes (inset of Figure 4(a)), either given in [R, Z] in Cartesian coordinates, or in [r,θ] in magnetic coordinates. The voxel center is at $\phi_{bol} = 108°$ while the two ends are at $\phi = 105°$ and 111°, respectively. For calculating the elements T_{ij} in the geometric matrix T (see Eq. (3)), each voxel is divided into segments (along the magnetic flux tube) due to variations in plasma cross sections. This is illustrated in Figure 4(a), taking the grid structures around the LCFS at $\phi = 105°$, 108° and 111° as examples. It is noticeable that the SOL grids (in blue in Figure 2(b)) are built up to a

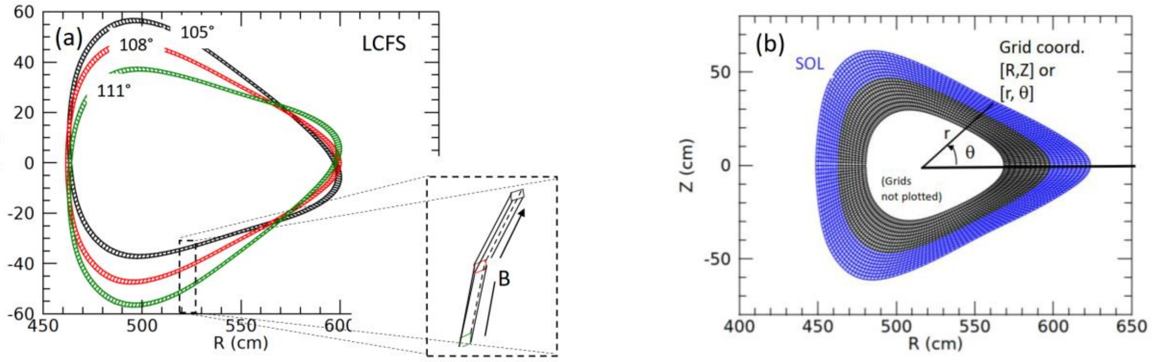

Figure 4. (a) The variation of the grids around the LCFS in the plasma cross section at $\phi = 105°$, 108°, and 111° in the field of view of the bolometers; they display the feature of stellarator symmetry around $\phi_{bolo} = 108°$ (in red). The inset shows the principle for building a voxel by connecting the 2D grid at different toroidal positions along the flux tube. (b) The 2D grids at $\phi = \phi_{bolo}$ created based on the magnetic vacuum configuration for SDC are with 200 poloidal grid points and 29 radial grid points. The confined plasma region (with 20 radial shells) is marked in black, the SOL (with 9 radial shells) in blue. Each grid center in Cartesian coordinates given in [R, Z] has its corresponding polar coordinates [r,θ].

normalized radius $r/a = 1.3$ (a stands for the minor radius of the LCFS), beyond which normally no plasma radiation can be detected.

The grids are coarser in the core ($\Delta r \sim 4$ cm) than at the edge ($\Delta r \sim 1.5$ cm) to ensure sufficient spatial resolution for the SOL plasma while maintaining a relatively low pixel number n_p. The emissivity variation in the toroidal extension is not resolvable, thus the effective toroidal resolution of the system is $\Delta\phi \sim 3°$.
In addition, to accurately calculate the geometric matrix T, the aperture and detector area are divided into segments (typically 4 each, above which no significant change in the calculated T occurs). The resulting sub-LoS set is further used to reduce numerical uncertainties originating from the finite LoS width.

One advantage of these flux-surface-based grids is to allow us to incorporate *a priori* knowledge of the expected solution or set reasonable constraints on plasma confinement features.

The optimization and the physical constraints. In view of the high pixel count of $n_p > 2000$ and much fewer available signals ($n_l = 65$), the tomography inversion turns into a poorly conditioned (underdetermined) problem. To solve such ill-posed problems, regularization techniques such as maximum entropy [47], Gaussian tomography [48], and minimum Fisher regularization (MFR) [34] have been widely applied. The MFR method was initially chosen for the W7-X bolometer tomography because of its advantages over other methods [49]. However, after preliminary tests with simple phantoms [33], we found that the reconstructed profiles (i.e. the tomograms) were not accurate enough, when we tested the algorithm by choosing radiation profiles from 3D modeling as phantoms. We also found that the weighting factor used in smoothing the searched emission profile affected the tomograms particularly, even when the goodness-of-fit χ^2 reaches ~1, which is defined as

$$\chi^2 = \frac{1}{n_l}\sum_l \frac{(\sum_i T(i,l)*\varepsilon(i) - P_l)^2}{\sigma(l)^2}, \tag{4}$$

where $\sigma(l)$ is the measurement error of the l-th signal and other parameters are as previously defined.

Our solution for the W7-X bolometer tomography is specified by the following aspects:

1) A novel regularization functional $I_F = \int (\frac{\nabla\varepsilon}{\varepsilon})^2 dV$ based on the relative gradient smoothing (by using the square of the sought emissivity as weighting factors) is implemented in the algorithm, replacing the usual Fisher information $I_F = \int \frac{(\nabla\varepsilon)^2}{\varepsilon} dV$.
2) Anisotropic smoothing in poloidal and radial directions [35] is implemented using parameters k_θ and k_r, respectively. Based on the fact that plasma emission is usually more uniformly distributed on the FS than in the radial direction, higher degrees of smoothing in the θ-direction are introduced, especially in the core $k_\theta/k_r >> 1$. Thus, the regularization functional I_F is split into two parts related to radial and poloidal gradients and expressed as follows:

$$I_F = \sum_{i=0}^{n_p-1} \frac{(k_r \nabla_r \varepsilon(i))^2 + (k_\theta \cdot \nabla_\theta \varepsilon(i))^2}{\varepsilon(i)^2}, \tag{5}$$

Usually, k_r is set to unity and k_θ is a radially dependent function that is optimized during code validation (typically k_θ =50 in the core and 20 at the edge). Keeping the minimization of the following function as [34]

$$\Phi = ½\chi^2+\lambda\cdot I_F, \tag{6}$$

where λ is a regularization parameter optimized during iterative smoothing of the emissivity profile, a solution is obtained when χ^2 ~1 is reached.

3.2 Code validation by phantom simulations

In order to validate the new reconstruction procedure under the most realistic conditions possible, dedicated 3D modeling of the radiation intensity distribution under real plasma conditions has been performed. This is done using the EMC3-EIRENE code [50], which is a combined 3D fluid and kinetic transport Monte Carlo code for the plasma boundary and has been widely used to study heat fluxes and impurity radiation within the SOL of inherently 3D devices [28, 51]. The computational domain is radially wide enough to cover the main radiation zone of low-Z impurities (in the outer plasma region $r/a > 0.7$). The code currently does not cope with particle drifts and no charge exchange between the neutral hydrogen and the impurity ions is considered.

The discharge chosen for 3D modeling is XP20171109.45 (see Ref.[30] and later in section 4) purely ECR heated with P_{ECRH} = 3 MW. The plasma radiation during the discharge varies from low to high radiation levels. The simulations are carried out under the following assumptions:

- Oxygen is the only impurity species. Its relative yield is linearly coupled with the bulk ion flux on the targets, while the total yield is controlled by the total radiation power P_{rad}.
- No error fields are considered.
- Both oxygen and hydrogen have the same perpendicular diffusivity of D = 0.5 m^2/s, while a cross-field heat conductivity of χ = 1.5 m^2/s is assumed for both electrons and ions.

Hereafter, the radiation loss fraction, $f_{rad} = P_{rad}/P_{ECRH}$, instead of P_{rad}, is used as a free parameter. The validation of the tomographic algorithm is then performed with the following steps:

i. Extraction of 2D emissivity distributions in the bolometer field of view (ϕ = 105°-111°) from the 3D results covering an entire field period ($\Delta\phi$ = 72°);
ii. Calculation of the emissivity $\varepsilon(r, \theta, \phi)$ in the voxel segments (dimension of order cm) by averaging the 3D modeling results over more than 50 finer cells (dimension of order mm);
iii. Computing the synthetic bolometer signals, using the averaged emissivity ε in the voxels and the prepared geometric matrix T, based on Eq. (3);
iv. Adding Gaussian noise to the synthetic signals with a level close to the real measurement errors (~3%; see section 2);
v. Setting smoothing factors that vary within a reasonable range by running the RGS algorithm to finally find the optimized factors as well as the reconstructions at the end.

As for the last point, the mean square deviation (MSD) defined as

$$MSD = \sqrt{\sum_j (\varepsilon_{rec,j} - \varepsilon_{phan,j})^2} \,/\, \sqrt{\sum_j \left(\varepsilon_{phan,j}\right)^2}, \tag{7}$$

is introduced to quantitatively qualify the reconstructions, where j stands for the grid index, and ε_{rec} and ε_{phan} are the local emissivity in tomograms and phantoms, respectively. At the same time, a comparison of the radial 1D profiles obtained by poloidal averaging over the 2D distributions in both phantom and tomogram is performed for an additional quality check (see Appendix).

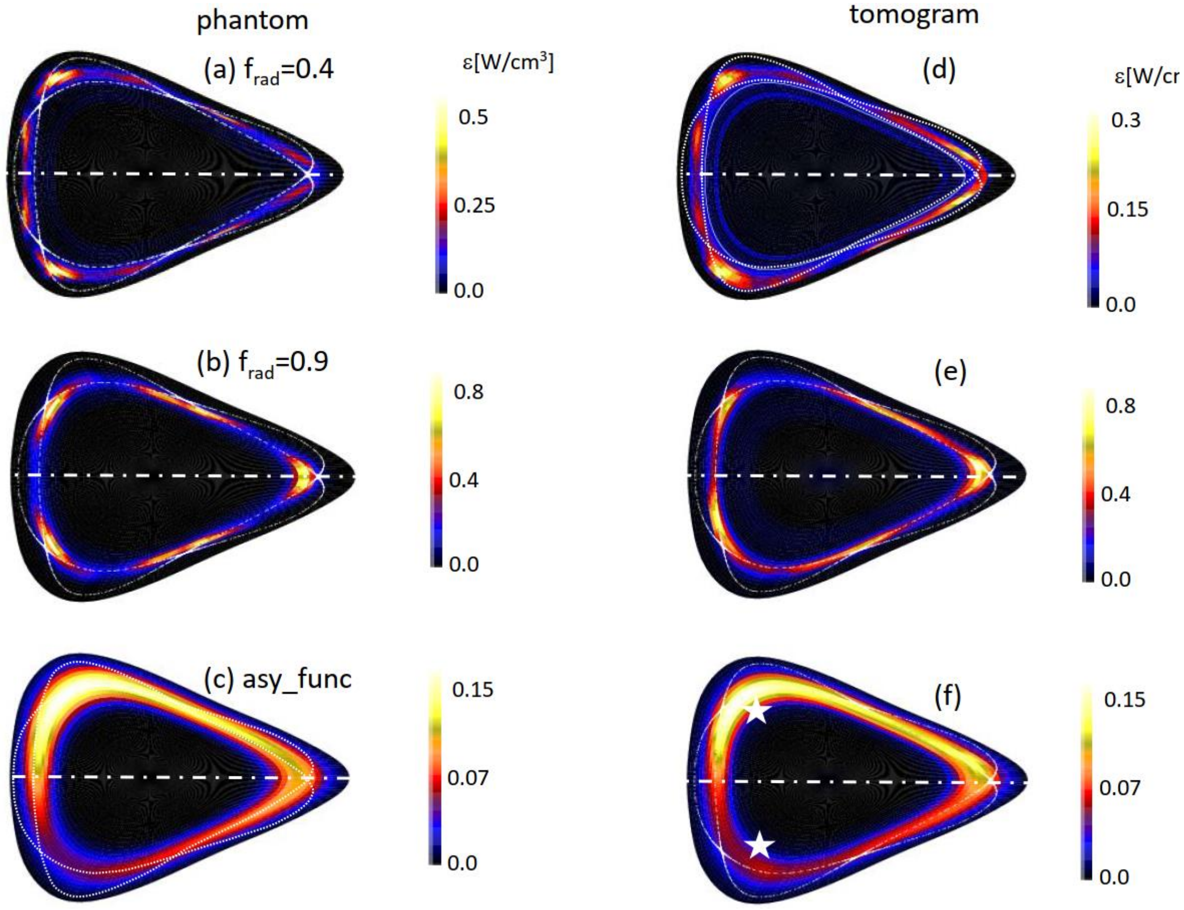

Figure 5. The 2D emissivity patterns of the oxygen impurity with up-down symmetry generated by 3D modeling using EMC3-Eirene code for f_{rad}=0.4 (a) and f_{rad} = 0.9 (b) are used as phantoms for validating the tomography algorithm. The tomographic reconstructions based on synthetic signals of HBC and VBC (assuming Gaussian noise with 3% relative error) using the RGS-method are shown in (d) and (e), respectively, (c) the phantom and (f) the reconstructions having an artificial up-down asymmetry for obtaining insight into the uncertainty of the algorithm in resolving up-down asymmetric distributions. The two stars in (f) exemplify regions with artifacts that lead to larger uncertainties in the derived asymmetry magnitude (see Figure 7). Note that the diagrams are scaled to the individual maximum emissivity in each tomogram for better visualization of the reconstruction structure.

These are executed for low, medium and high radiation scenarios with f_{rad} = 0.4, 0.8 and 0.9, respectively. It is found that (setting k_r=1) the smoothing factor k_θ in the range of 20-60 can produce similar well-qualified reconstructions with low *MSD* values (<0.2). Figure 5 shows the phantoms and the reconstructions in (a-b) and (d-e), respectively, using the low and high-f_{rad} cases as examples. They are all presented in the 2D grids at the toroidal plane ϕ_{bolo} in the Cartesian coordinates.

The diagrams in Figure 5 already show a good match between phantoms and reconstructions. Although some local differences are visible (e.g., the lower maximum emissivity of ~0.3 W/cm^3 in Figure 5(d) compared to ~0.5 W/cm^3 in Figure 5(a), indicating the smearing of the phantom by the reconstruction), the main features of the oxygen radiation, such as the edge-localized radiation zone and the up-down symmetry in the radiation distribution (with an uncertainty of ~3% as assumed errors) are reproduced. The symmetry is also evident in the synthetic HBC signals, which have symmetric LoS coverage (see Section 2). The signals (based on the phantom for f_{rad} = 0.9) are exemplified in Figure 6 (background in green for the HBC and in blue for the VBC). It shows the up-down symmetric chordal brightness of the HBC with ch16 and ch17 viewing the plasma center. Channels viewing the LCFS measure high signals, additionally, there are recognizable "bumps" in the profiles that come from channels observing brighter radiation zones in the magnetic islands (marked by star symbols). Also shown in Figure 6 are the backwards-calculated signals using the tomogram, which match the synthetic signals within the error bars, demonstrating good agreement (χ^2~1).

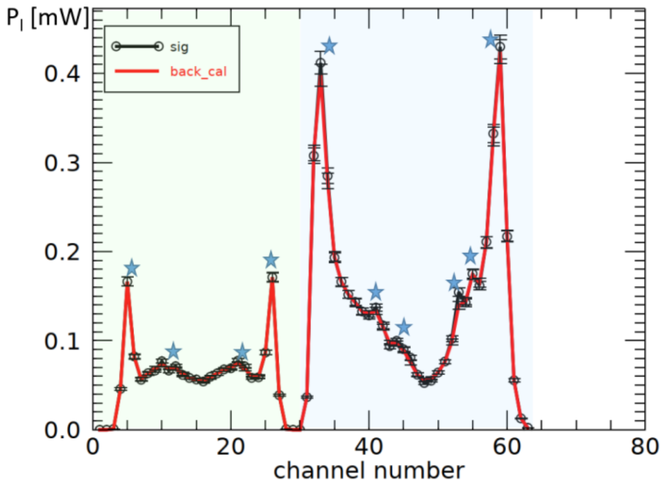

Figure 6. The synthetic signals for the HBC and the VBC based on EMC3-EIRENE simulated oxygen radiation distribution in Figure 5(b) (open circles) versus the backward-calculated ones based on the tomogram in Figure 5(e) displays the goodness of the reconstructions. The error bars correspond to 3% relative errors. The 'stars' indicate the channels viewing island radiation.

An example of the superiority of the RGS method over the MFR method in dealing with W7-X bolometer tomography can be found in the Appendix.

3.3 Resolving radiation asymmetry

The EMC3-EIRENE code produces up-down symmetric radiation distributions in the plasma cross section under consideration as shown in Figure 5 (a) and (b). Since up-down asymmetry is observed in the experiments, we further investigate the capability of the algorithm for the bolometer tomography using a phantom with an artificial asymmetric radiation pattern. The function to generate the phantom is $\varepsilon(r,\theta) = \varepsilon_0 e^{-\frac{(r-r_p)^2}{r_w^2}}(1 + f_a y(\theta))$, which contains an asymmetric function of the poloid angle $1 + f_a y(\theta)$ multiplied by an exponential function

$\varepsilon_0 e^{-\frac{(r-r_p)^2}{r_w^2}}$, where y(θ) is a sinusoidal-like function but enforces a maximum and minimum at 130° and 225° to mimic the experimentally observed asymmetry, as in Figure 10 (f), f_a= 0.55 is the magnitude of the asymmetry assumed; in the radial function, ε_0 = 0.5 W/cm^3 is taken, r_p = a is the radial peak position, r_w =0.15a is the width of the radiation zone and a = 52.2 cm is the minor radius of the plasma.

This phantom is shown in figure 5 (c). An emissivity variation is defined by

$$\tilde{\varepsilon}(r,\theta) = \frac{\varepsilon(r,\theta) - <\varepsilon(r,\theta)>}{<\varepsilon(r,\theta)>}, \tag{8}$$

where $< \varepsilon(r,\theta) >$ is the poloidally averaged emissivity. The asymmetry magnitude f_a is the magnitude in $\tilde{\varepsilon}(r,\theta)$, which has a maximum at θ= 130° and a minimum at θ= 225°.

The reconstruction is performed using the same procedures and smoothing factors by validations described beforehand. The obtained tomogram is shown in figure 5 (f), which reproduces the up-down asymmetry in the phantom well. Furthermore, the emissivity variations $\tilde{\varepsilon}(r,\theta)$ are derived (for r/a = 0.9-1.0), and are shown in Figure 7. Also shown there is the variation $\tilde{\varepsilon}(r,\theta)$ from the phantom for comparison. The asymmetry magnitude in the phantom is $\tilde{\varepsilon}$ = 0.55 (see the dotted red line) as given while those from the reconstruction varies from 0.3 to 0.6 showing an average uncertainty of about 20%. The poloidal positions where the maximum and minimum emissivity occurs, deviates from that in the phantom with an uncertainty of 25%. These deviations are due to the finite error bars given in the synthetic signals and numerical noise. It is observed that at radial positions with relatively weak (absolute) emissivity, e.g. r/a=0.88 (the black curve), higher deviations in the magnitude of the asymmetry are obtained, which are correlated with the artefacts in the tomogram (see the regions close to the stars in Figure 5 (f) with visible smeared emissivity gradient). This test confirms that the bolometer tomography is capable of resolving the asymmetry in the radiation distribution and both magnitude and phase can be resolved within an uncertainty of about 20-25%.

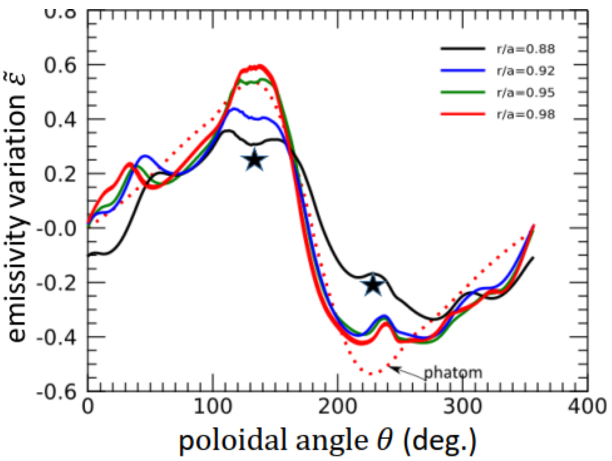

Figure 7. A comparison of the poloidal emissivity variation derived from the phantom (the dotted red line) and the tomogram (the solid color lines), which are shown in Figure 5 (c and f), respectively. The two stars indicate the local positions with relatively large uncertainty in the $\tilde{\varepsilon}$-value, which correspond to the regions with artefacts also marked by two stars in Figure 5 (f).

4. Experimental results

The data points marked with star symbols in Figure 3 are chosen for demonstrating the features of the 2D radiation distributions in W7-X plasmas (OP1.2a). They are from two experimental programs (XP20171109.45 and XP20171206.37), in which comprehensive radiation scenarios for the normal (SDC+) and reversed magnetic field (SDC-) configuration are covered.

The plasmas in these two experiments, hereafter abbreviated as XP45 and XP37, are both heated with P_{ECRH} =3 MW. The time traces of the relevant diagnostic measurements are shown in Figure 8, in the left panels for XP45 and in the right panels for XP37. The density increase in XP37 is achieved by gas fueling only while in XP45 with additional pellet injections (from t = 1.7 s to 2.1 s). Generally, with increase of the line averaged density $<n_e>$ (measured by the interferometer [52]) the plasma radiated power P_{rad} increases. P_{rad} is obtained by linearly scaling the radiated power falling within the field of view of the HBC to the total plasma volume (neglecting toroidal variations) [30]. In the later phases of both discharges, the radiated power fraction f_{rad} = P_{rad}/P_{ECRH} (with an uncertainty of ~10%), reaches levels close to unity, designating plasma detachment [30]. The edge plasma density and temperature, measured by Thomson scattering [53], reach $n_e(0.9)$~2-2.5 ×10^{19} m^{-3} and $T_e(0.9)$~150 eV for a normalized radial position r/a = 0.9 (open circles). Close to the LCFS (r/a ~1; solid circles) the values n_e are only slightly lower, while the values T_e show a visible reduction (down to ~50 eV) despite the scattering in the data points. During the experiments, the effective ion charge Z_{eff}, derived from the visible spectrometer measurements [54], varies from ~2 to ~5, which is related to the impurity transport associated with gradients in the profiles and also boundary plasma

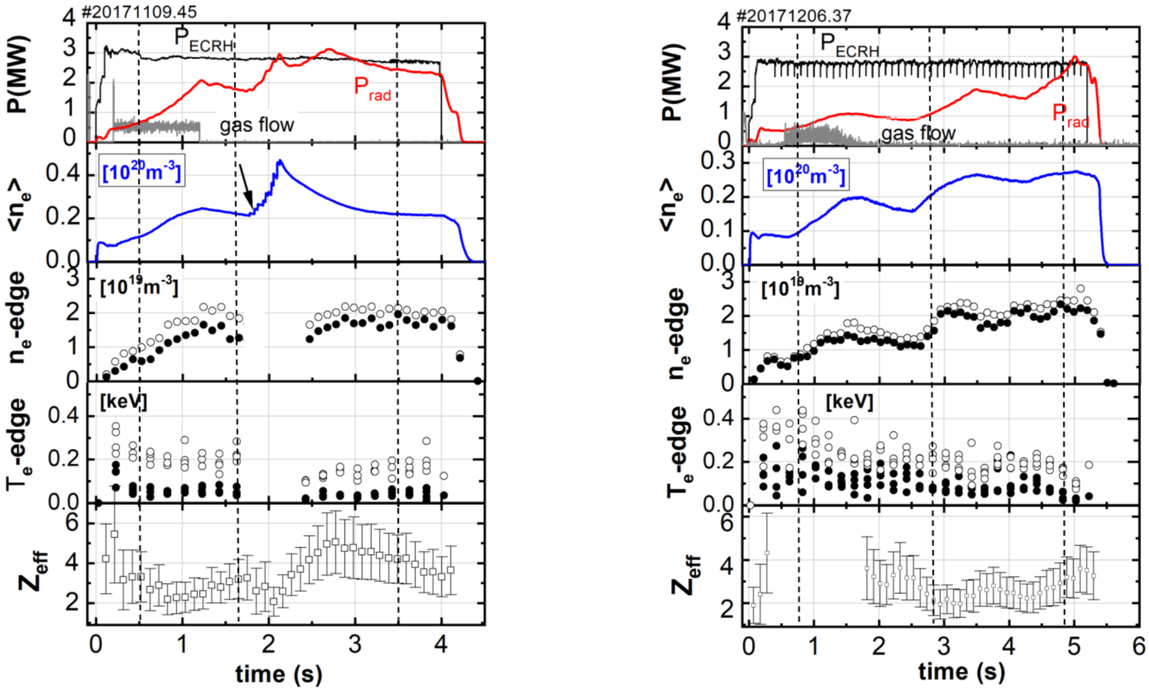

Figure 8. Time traces of diagnostics in the representative experiment programs, XP45 for SDC+ (left panels) and XP37 for SDC- (right panels). Shown are, from top to bottom, the ECRH power P_{ECRH}, total radiative power loss P_{rad}, the gas flow for plasma fueling, line-averaged plasma density $<n_e>$ from the interferometer, the edge plasma density and temperature (for r/a = 0.9 in open circles and r/a ~1 in solid circles), from the Thomson scattering, and the ion effective charge Z_{eff} from the visible spectrometer. The data points of T_e and n_e for t =1.7 s to 2.4 s in XP45, and Z_{eff} for t = 0.5 s to 1.7 s in XP37 are not available due to interference of pellets and gas fueling on the diagnostics, respectively. The dashed vertical lines mark the selected time points for performing bolometer tomography.

parameters (see later in this section). For the discharges under consideration (no wall boronisation), oxygen ions such as OVI are the predominant radiators [30].

The asymmetries in the impurity radiation have been initially observed in the temporal evolution of the chord brightness profiles measured by the HBC. At the selected time points (indicated by the vertical dashed lines in Figure 8) they are illustrated in Figure 9 (a) and (b) for XP45 and XP37, respectively. They correspond to the low, medium, and high radiation scenarios with f_{rad} = 0.25, 0.6, and 0.9, and the corresponding plasma densities (in units of 10^{19} m^{-3}) in these scenarios are $\langle n_e \rangle$ = 1.0, 2.2 and 2.2 in XP45, and 1.0, 2.0 and 2.5 in XP37. Note that in XP45, the radiative loss fraction f_{rad} increases from 0.6 to 0.9 after pellet injections despite the same line-averaged density, which is explained by the increase in plasma density and the decrease in temperature around the LCFS (cf. [30]). It can be clearly seen that, except in the cases with the lowest f_{rad}, the profiles are not symmetrical around the two central channels ch16 and ch17 (see Figure 2) near the vertical dashed lines: in the XP45, the lower plasma region emits more intensivly, typically recorded by ch25-27 (note that ch27 views the lower LCFS). In XP37, the upper plasma region emits more intensively, typically recorded by ch6-8 (note that ch6 views the upper LCFS). As f_{rad} increases, the up-down asymmetry becomes more pronounced. The "bumps" on the profiles (with magnitudes significantly larger than the measurement error bars) occurs normally for high-f_{rad} cases, characterizing the non-uniformly distributed impurity radiation in the SOL. This is more clearly seen in the 2D radiation distributions in Figure 10.

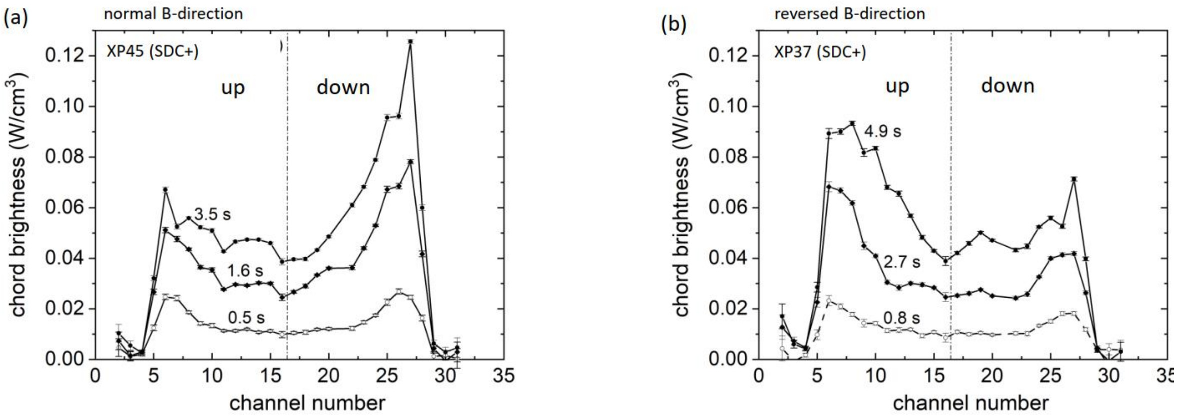

Figure 9: Evolution of the chord brightness profile and its asymmetry from HBC measurements in XP45 (a) and XP37 (b) in the normal and reversed B-field directions. The time points are the same as indicated by the dashed vertical lines in Figure 7 corresponding to low (f_{rad} = 0.25), medium (f_{rad} = 0.6) and high-radiation (f_{rad} = 0.9) scenarios. The error bars based on the standard deviation of the measurements are also shown.

Tomographic reconstructions. The 2D radiation profiles in the plasma phases described in Figure 9 have been obtained using the RGS method based on the HBC and VBC measurements. The obtained results are shown in the 2D grids at ϕ_{bolo} in Cartesian coordinates $[R, Z]$ in Fig. 10 (left panels for XP45, right panels for XP37). A clear feature in the radiation distributions is that for all plasma scenarios most of the radiated power originates from the plasma edge ($r/a >$ 0.8). These edge-localized low-Z impurity radiation features are also predicted by the 3D modeling (see Figure 5 (a) and (b)), but the tomographic reconstructions based on bolometer measurements show the following particular phenomena:

1. In the low-density, low-f_{rad} scenario (Figure 10(a) and (d)), the emissivity is almost uniformly distributed around the LCFS and the structure of the individual islands is not very pronounced. The power radiated from the confined plasma region $P_{rad,core}$, obtained by integrating the emissivity within the LCFS, gives a radiative power fraction $f_{rad,core} = P_{rad,core}/P_{rad}$ of ~60% for both discharges, which is higher than that for the higher f_{rad} cases (~50%) as in Figure 10 (b) and (e). The relative reduction of impurity radiation from the core at medium f_{rad} is also observed in discharges conducted after wall boronization, which have a lower Z_{eff} value, usually below 1.5 [55]. We believe that the evident core impurity radiation in Figure 10(a) and (d) is related to the weak screening effects of the magnetic islands on both impurities and neutral hydrogen at the low edge densities of 0.6-0.8×10^{19}

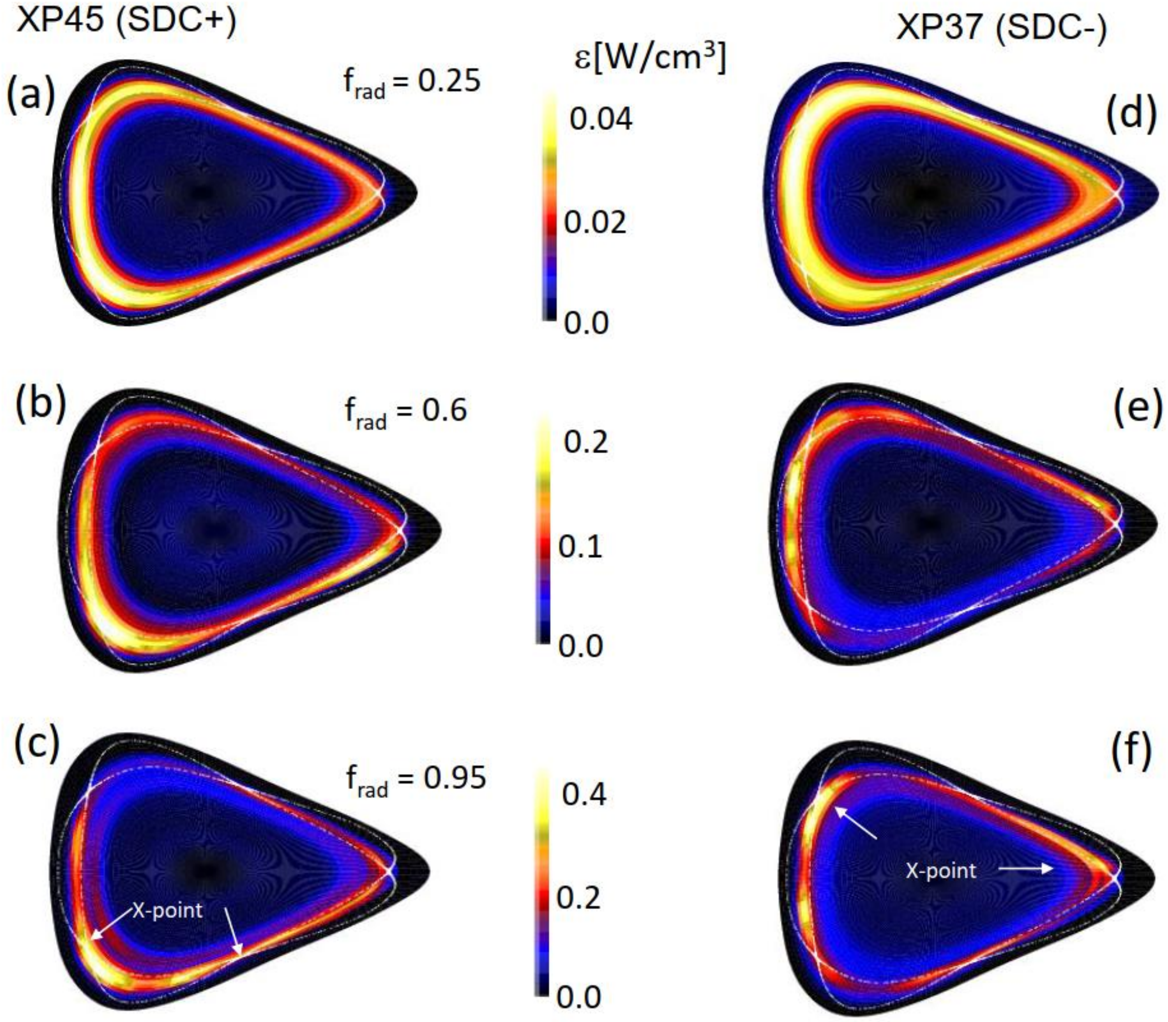

Figure 10. Evolution of the 2D radiation intensity distributions obtained by bolometer tomography using RGS-method in discharge XP45 (left panels; SDC+) and XP37 (right panels; SDC-) showing a magnetic field direction dependent asymmetry in impurity radiation. The selected time points are the same as those in Figure 8 (also marked by vertical dashed lines in Figure 7). The separatrix from the ideal vacuum field is shown in white lines.

m^{-3} (see Figure 8) [28]. The neutral hydrogen backscattered from the targets is energetic (above several tens of eV) and has a long mean free path (in the range of meters to several hundred meters). This enters the core and subsequently undergoes charge exchange (CX) collisions with the impurity ions, which further enhances the radiation inside the LCFS. As a result, the radiation patterns differ from the 3D modeling, as shown in Figure 5(a), which does not consider the CX collisions.

2. With increasing density and f_{rad} (Figure 10(b-c) and (e-f)), the 2D emission patterns become much more pronounced, characterized by a poloidal and radially varying structure in the outer plasma region ($r/a > 0.8$), overlaid by magnetic island radiation near the separatrix (shown with white lines). The up-down asymmetry seen in the chord brightness profiles in Figure 9 is now revealed. The emissivity comes from the regions around the five magnetic islands, unevenly distributed with higher intensity below the mid-plane in the SDC+ case (Figure 10(b-c)), but above the mid-plane in the SDC- case (Figure 10(e-f)).
3. The difference between the two higher density scenarios with $f_{rad} = 0.6$ and 0.9 lies in the poloidal locations of the maximum emissivity, a prominent feature of the 2D radiation distributions. It has been observed that, for $f_{rad} = 0.9$ to unity (plasma detachment), the intense radiation condenses around certain X-points, depending on the magnetic field direction and the plasma parameters. The radiative X-points are found here around the two lower X-points ($\theta = 216°$ and $288°$) for XP45 (Figure 10(c)) in the normal magnetic field direction and around the upper X-points ($\theta = 0°$ and $144°$) for XP37 (Figure 10(f)) in the reversed magnetic field direction. The radiation zone around the upper-X point in XP37 shifts radially inward while the lower one in XP45 does not. Understanding the X-point radiation behavior requires further analysis. Note that the intense emissivity around the lower X-point at the inboard side is also seen for $f_{rad} = 0.6$ in XP45, which is not yet understand. The more pronounced up-down asymmetries for $f_{rad} = 0.9$ than that at the lower $f_{rad} = 0.6$ is revealed by the more distinctive upper- and lower X-point radiation. In particular, the emission zone within the LCFS with weaker intensity also varies in poloidal direction.

Analysis of the radiation asymmetry. In the following, the magnitudes of the radiation

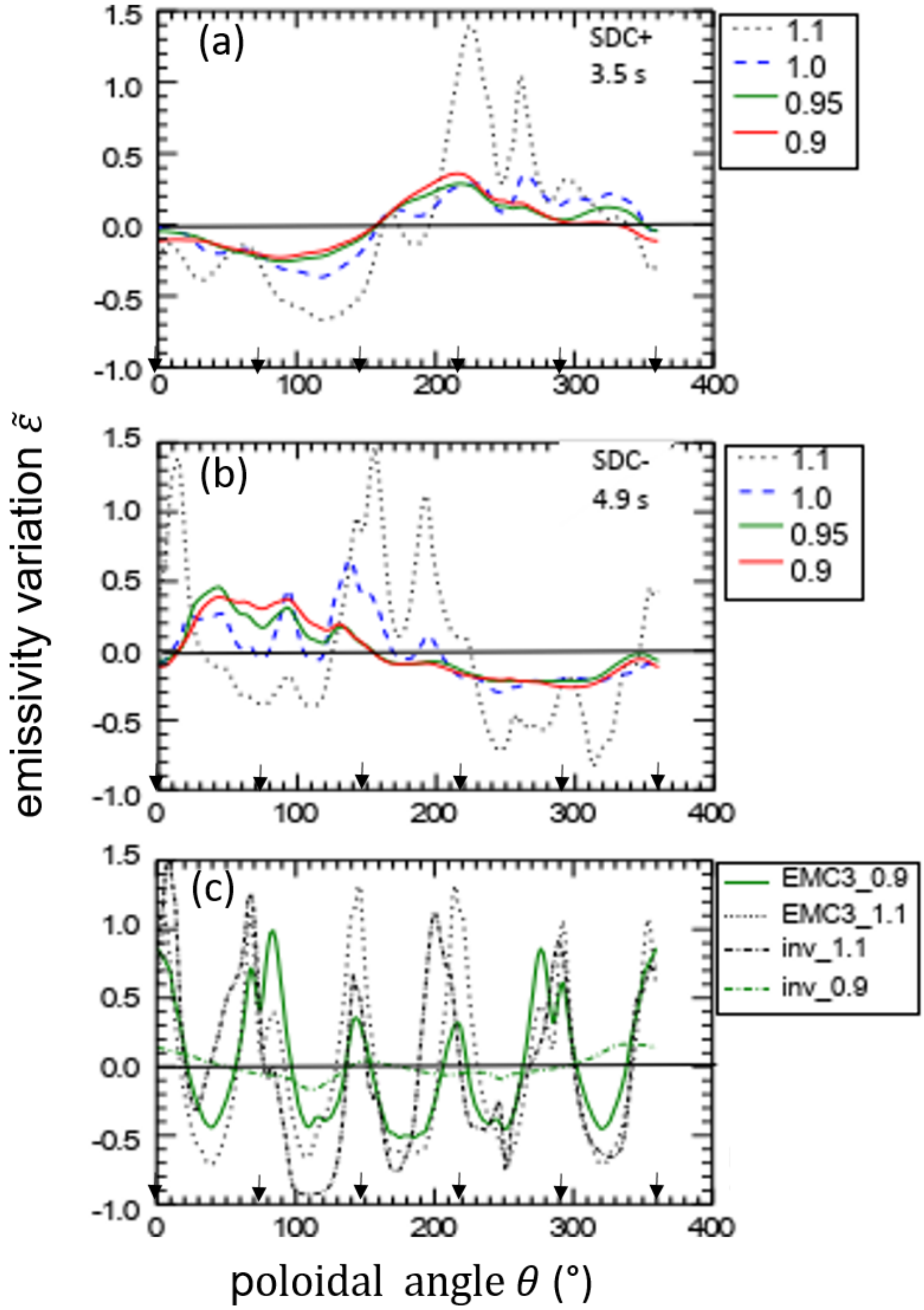

Figure 11. A comparison of the emissivity variation $\tilde{\varepsilon}$ on the FS for r/a=0.9, 0.95 (in red and green, respectively) for the high-f_{rad} scenarios in XP45 (a) for SDC+ and XP37 (b) for SDC-. Also shown are the SOL emissivity variations in the θ-direction (in dotted black line) with peaks at $\theta \sim 10°$ and 145° (SDC- case) and 220° (SDC+ case) near the X-points (marked by arrows on the θ-axis) above and below the plasma mid-plane, respectively. The data on the LCFS (in dashed blue) is not further treated. (c) The poloidal variation of the emissivity $\tilde{\varepsilon}$ based on the EMC3-EIRENE modeling results (Figure 5(b)) to represent an up-down symmetric case; Also the tomographic reconstruction results (Figure 5(e)) are included to illustrate the uncertainty of the reconstructions. Only two radial positions (r/a=0.9 and 1.1) are chosen to keep the plots more legible.

variation in the poloidal direction are derived taking the high-f_{rad} cases as generic case. The poloidally-averaged emissivity $<\varepsilon>$ is first calculated by poloidal integration of the $\varepsilon(r,\theta)$ values in the grids of each radial position and normalized by grid area summation. Subsequently, the relative emissivity variations $\tilde{\varepsilon}(\theta) =(\varepsilon(r,\theta)-<\varepsilon>)/< \varepsilon>$ in the poloidal direction are calculated. The obtained results (for f_{rad} = 0.9) for the outer plasma region of interest are shown in Figure 11 (a) and (b) for XP45 and XP37, respectively. In addition, Figure 11(c) shows the poloidal variation of the emissivity $\tilde{\varepsilon}$ for two selected radial positions based on the EMC3-EIRENE modelling results (Figure 5(b)) and the tomographic reconstruction results (Figure 5(e)) to represent an up-down symmetric case. The following observations are made:

a) The variation $\tilde{\varepsilon}(\theta)$ inside the LCFS is sine-shaped, indicating an up-down asymmetry. For XP45, the peak of $\tilde{\varepsilon}(\theta)$ is at $\theta \sim 210°$, while for the XP37, it is at $\theta \sim 40°$- 90°; The wider θ range is likely due to reconstruction uncertainty as previously indicated for phantom simulations. The phase difference between $\tilde{\varepsilon}(\theta)$ for XP45 and XP 37 is not exactly 180°, but a reversal of the asymmetry is clearly observed. Those at r/a = 0.9 and 0.93 (red and green lines, respectively) yield an asymmetry magnitude of $\tilde{\varepsilon}_{\mathrm{m}}$~0.3. The differences between the curves reflects the result uncertainty (~20% cf. also section 3.3).

b) For r/a =1.1 (in the SOL) $\tilde{\varepsilon}\ (\theta)$ is not sinusoidal and the variation magnitude is much larger ($\tilde{\varepsilon}_{\mathrm{m}}$~1.5). Multiple peaks appear at the θ-angles near the X-points at multiples of θ = 72°. These X-points, either in the lower (for SDC+) or upper (for SDC-) plasma region, are those which are poloidally closest to the emissivity peak within the LCFS, indicating a direct relationship. Note that the data on the LCFS (in dashed blue) mixes with those inside and outside the LCFS and they are not further discussed.

Similar analyses have been performed for lower density, lower f_{rad} scenarios. For f_{rad} = 0.6 in XP45 and XP37, in addition to an asymmetry reversal in the poloidal variation similar to that described previously, the asymmetry magnitudes are reduced to $\tilde{\varepsilon}_{\mathrm{m}}$~0.2 inside the LCFS ($r/a$ = 0.9) and $\tilde{\varepsilon}_{\mathrm{m}}$~0.8 for the SOL ($r/a$ = 1.1), both lower than in high-density, high-radiation scenarios. This is consistent with the general observation in Figure 3, which shows a reduction in radiation asymmetry with decreasing density.

5. Discussion

The above analysis of the poloidal variations in the 2D emission profile from the bolometer tomography provides a quantitative observation of the radiation asymmetry in W7-X. The asymmetry inside the LCFS suggests that impurities might be non-uniformly distributed on the flux surface. This will be discussed in the following.

Correlation of radiation asymmetry with impurity asymmetry. The local emissivity $\varepsilon(r,\theta)$ measured by the bolometers is mainly due to the line emissions from impurity ions (such as OVI). The emissivity is proportional to the impurity density n_z [56, 57] as

$$\varepsilon = n_e n_z L_z\,(Z, T_e), \tag{9}$$

where L_z is the electron temperature dependent radiation loss function of the impurity with atomic number Z. Within the LCFS, assuming that T_e and n_e are constant on the flux surface, the emissivity variation on the flux surface is proportional to the impurity density variation

$\widetilde{n_z}(\theta) \approx \tilde{\varepsilon}(\theta)$. The n_z variation magnitude is then ~0.3 at r/a = 0.9-0.95 for both SDC+ and SDC- plasmas (in the high radiation scenarios).

This result is supported by the measurements from the soft X-ray (SXR) camera system at W7-X [44]. They are equipped with filtered AXUV-22EL photodiode arrays, sensitive to high-energy bremsstrahlung (photon energy >500 eV). The cameras monitor another triangular plasma cross-section (at toroidal angle ϕ=36°) which matches that monitored by the bolometers (at toroidal angle ϕ=108°). Two cameras (2D and 3B) have been chosen to examine possible up-down asymmetry. They view the plasma from the inboard side, having geometrically up-down symmetric LoS distribution. In XP45, it has been observed that the signals of the two camera channel (noted as ch) pairs 161/200, and 160/201, which view the upper and lower edge plasma with a tangential radius of 0.95 and 0.9, respectively (see Figure 12 (a)), deviate from each other as the plasma density increases, which supports an up-down asymmetry. The time evolution of these channel signals in XP45 is shown in Figure 13 (b). The data points of ch200 (in red line) and ch201 (in red open circles) are greater than those of ch161 (in black line) and ch160 (in black open circles) for t > 2.0 s. The SXR emission below the mid-plane is more intensive than above the mid-plane in the later phase with high-f_{rad} (cf. also Figure 9). In contrast, for XP37 with reversed magnetic field direction the upper plasma emits stronger SXR than the lower plasma, which is shown in Figure 12 (c) by comparing the signals of ch160 (in black open circles) and ch201 (in red open circles) for t > 3.5 s and the signals of ch161 (in black line) and ch200 (in red line) for t > 4.5 s.

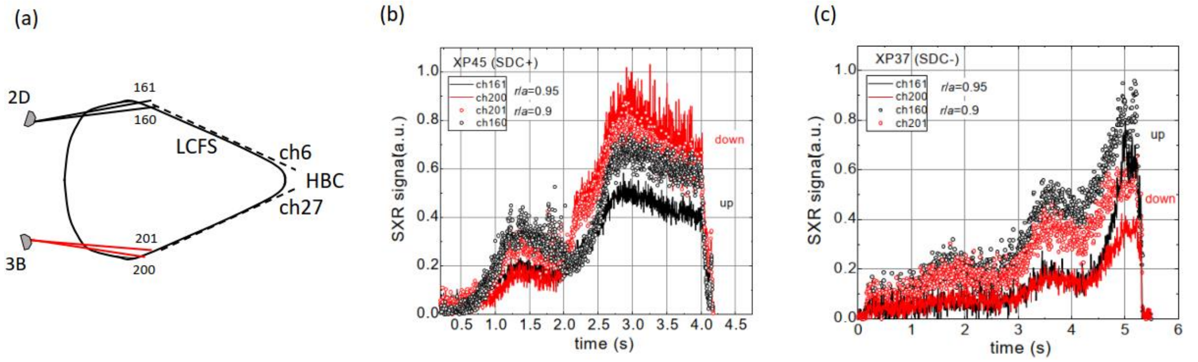

Figure 12. (a) The selected SXR camera channel pairs, channel 160/210 and channel 161/200, with up-down symmetric LoS viewing the triangular plasma cross section from the inboard side with a tangential radius of r/a=0.90 and 0.95, respectively. (b) In XP45 (t > 2.0 s), the lower plasma region emits stronger SXR than the symmetric upper region, shown by measurements of ch201 and 200 (in red) and ch160 and 161 (in black), respectively. (c) In XP37 (in the reversed magnetic field direction), the lower plasma region (r/a=0.9) emits weaker SXR than the symmetric upper region, shown by measurements of ch201 and 160 for t > 3.5 s; that of ch200 and 161 occurs in the later phase for t > 4.5s. They show that the up-down asymmetry of the impurities is correlated with the magnetic field direction, supporting the bolometer results.

Since no high-Z elements were observed in the studied plasma, the SXR channels actually measure bremsstrahlung and soft X-ray emission (partly due to the optical filter used) from highly charged ions such as OVII (z = 6), since OVII is the ion with the highest fractional abundance at the plasma edge, where T_e is ~100 eV [57]. With the same assumption as before, that n_e and T_e are constant on the flux surface, we can expect asymmetry in the impurity density.

Using the ratio of the upper and lower channel signals f_{ud}, a line-averaged-asymmetry magnitude in the outer confined plasma region can be defined as $f_{asy} \equiv 2.|(1-f_{ud})|/(1+f_{ud})$ and we obtain $f_{asy} = 0.5\pm0.1$ and 0.3 ± 0.1 for $t = 3.5$s in XP45 and $t = 4.9$ s in XP37, respectively. This result is qualitatively consistent with the bolometer results shown in Figure 11.

Furthermore, we find that the conditions for developing an impurity asymmetry based on neoclassical transport theory are satisfied according to our following estimates.

Theoretical considerations. According to neoclassical theory, the particle flux is determined by thermodynamic forces and frictional forces acting on ions as they move along magnetic field lines. These forces are related to the radial density and temperature gradients of the species and the electrostatic potential. Among all forces, the ion-impurity (*i-z*) friction force [58], $R_{zi\parallel} \sim m_i n_i \nu_{iz} \delta_{Pi} v_{thi}$, with ν_{iz} being the collision frequency between the background bulk ions and the impurity ions, plays a key role in the parallel transport of impurities in driving large amplitude asymmetries [5-7, 9, 15]. It has been shown in tokamaks that the poloidal variation in the impurity distribution (with charge z) is typically on the order of [58]

$$\tilde{n}_z/n_z \sim \epsilon\ \delta_z, \tag{10}$$

where ϵ is the inverse aspect ratio, $\delta_z \equiv \delta \nu_i^* z^2$ is the strong ordering parameter with ν_i^* the ion collisionality, and $\delta \equiv \rho_\theta/L_\perp$ is the expansion parameter, with ρ_θ the poloidal ion gyro-radius and $L_\perp$ the radial scale length associated with the density and temperature profiles. If $\delta_z \sim O(1)$, impurity density variation on the flux surface is developed. In large aspect ratio tokamaks it can be described by analytical formulas under certain assumptions [5, 7, 9].

In contrast, in stellarators such as W7-X, no analytical formulas exist for describing the impurity asymmetry up to now due to the complex 3D magnetic structure. The flux of the Pfirsch–Schlüter impurities ($\nu_z^* > 1$) such as the low-Z impurity at the plasma edge is expressed as [59]

$$\Gamma_z = \frac{1}{Ze}\langle uBR_{zi\parallel} + (p_{z\parallel} - p_{z\perp})\frac{\nabla_\parallel (uB^2)}{2B}\rangle,$$

where B is the magnetic field strength, u is a geometry-dependent quantity related to the magnetic field structure (its gradient along the magnetic field is $\nabla_\parallel u = \frac{2}{B^2}(b \times \nabla\psi) \cdot \nabla lnB$, with ψ standing for the radial spatial coordinate and b the unit vector along the magnetic field.). Γ_z is dominated by the first term related to the *i-z* friction force $R_{zi\parallel}$ (tokamak-like). The second term, related to pressure anisotropy (which can be neglected in tokamaks), i.e., the difference between parallel and perpendicular pressures, $p_{z\parallel} - p_{z\perp}$, is small but important for determining the radial electric field, which causes E×B rotation within each flux surface. The poloidal and toroidal distribution of impurities over the surface is determined by this rotation and by the *i-z* friction force, which governs the flow of impurities along the field. If this friction force is small enough, the impurities will be evenly distributed over each flux surface, but if it is large enough the impurity density will vary with the poloidal and toroidal angles [60]. This will generally be the case if the collisionality is high enough and the estimates below suggest that W7-X plasmas are indeed in this regime.

a) ***Collisionality:*** The ion collisionality at W7-X is calculated using $\nu_i^* = \frac{R}{\iota}\frac{\nu_i}{v_{th,i}}$ [61], where $v_{th,i}$ is the thermal velocity, ν_i is the total ion collision frequency, i.e., $\nu_i = \nu_{ii} + \nu_{iz}$ where $\nu_{ii} = n_i e^4 ln\Lambda/(4\pi\epsilon_0^2 . m_i^2 v_{th,i}^3)$ is the bulk ion self-collision frequency, and $\nu_{iz} = \nu_{ii} \cdot \sum_z \frac{z^2 n_z}{n_i} = (Z_{eff} - 1)\nu_{ii}$ is the *i-z* collision frequency related to the *i-z* friction force. Taking the W7-X plasma parameters at high radiation levels as an example Z_{eff} = 3.0-4.0 (at t = 4.9 s for XP37 and t = 3.5 s for XP 45 as shown in Figure 8), the major radius R = 5.5 m, the rotational transform ι = 1, T_e = 50-150 eV for r/a = 0.9-1, and assuming $n_i \approx n_e = 2\times10^{19}$ m^{-3} and $T_i = T_e$ at the plasma edge, we obtain ν_i^* = 0.5-2.

b) ***The poloidal ion gyro-radius:*** The value ρ_θ is related to the poloidal field B_p and the ion thermal velocity $v_{th,i}$ by $\rho_\theta \equiv m_i v_{th,i}/B_p$. According to the magnetic field structure in the studied triangular cross section of W7-X, B_p varies from 0.1 T to 0.3 T in the poloidal direction at the edge. An averaged value of B_p = 0.25 T is taken and one obtains ρ_θ= 0.6-1.0 cm for T_e varying from 50 to 150 eV.

c) ***The gradient length at the edge:*** We take $L_\perp = \left(\frac{1}{n_e}\frac{dn_e}{dr}\right)^{-1} \approx$ 10 cm based on the density profile at t = 3.5 s in XP45 [30], and considering z = 6 as OVII has the highest fractional abundance in the considered T_e range [57] and obtain $\delta_z \equiv \nu_i^* z^2 \rho_\theta / L_\perp \approx$ 1-5. We note that there is a large uncertainty due to diagnostic limitations.

These estimates show that (I) the ions are collisional in the studied plasma, (II) the frequency of *i-z* collisions exceeds that of *i-i* collisions by a factor of $Z_{eff}-1 > 2$, such that the impurities affect the kinetics of the bulk plasma, (III) the resulting parameter δ_z is greater than 1, satisfying the condition for developing an impurity asymmetry according to neoclassical theory (see above).

The impurity asymmetry is related to the poloidal component of the magnetic field B_p as also expressed by the analytical solutions for tokamaks [5, 7]. When the toroidal magnetic field is reversed, B_p reverses accordingly which results in a reversal of the impurity asymmetry. The magnitude of the asymmetry is related to *i-z* collision frequency and the asymmetry develops consequently at the edge where T_e is low and low-Z impurities are abundant. Here, the high Z_{eff} in OP1.2a (before wall boronisation) is an important factor. Furthermore, the radial temperature gradient can influence the magnitude and possibly even the sign of the friction force [60], thereby also the sign of the up-down asymmetry. On W7-X, a reversal of the sign of the asymmetry has been observed during some discharges (see Figure 3) without changing the direction of the magnetic field when the plasma becomes smaller than usual. Detailed studies of this phenomenon and the search for the connection with the temperature gradient is subject to future work.

Asymmetric impurity flow to the SOL. The impurity asymmetry that occurs in the outer confined plasma region implies asymmetric impurity flow from the plasma core to the SOL, indicating asymmetric impurity cross-field transport. This result provides additional information on W7-X impurity transport in the confined plasma region, which has been primarily investigated with active impurity injections (e.g., laser blow-off), and yields a flux surface-averaged 1D transport coefficient (much larger than that predicted by neoclassical theory in common ECR-heated plasmas) [62-64].

In the W7-X SOL the connection length is on the order of meters to several hundred meters. Parameters such as density n_e and temperature T_e, which are determined by the power and particle balance, are also associated with boundary conditions such as impurity sources, particle drifts, and error fields. They typically vary in both poloidal and toroidal directions. We have observed that the emissivity variations in the SOL are much larger than those on the flux surfaces within the LCFS (as shown in Figure 11). This enhancement is considered to be related to additional T_e variation, since a higher local radiation intensity (due to a higher impurity flux from the interior of the LCFS) corresponds to a stronger cooling of the local temperature, which in turn further raises the impurity emissivity (due to $dL_z/dT_e < 0$ in eq. (9)).

Final remarks. It is worth noting that the magnetic configuration at W7-X (even for the vacuum fields without finite beta effects) has uncertainties because of the existence of (small) error fields [65, 66]. This may affect the toroidal symmetry in the W7-X SOL for parameters such as divertor target heat and particle loads, which in turn yield spatially varying impurity sources. In addition, drift effects, which have already been observed in W7-X [67], can also contribute to asymmetries in impurity sources and plasma parameters. The radiation asymmetry observed by the bolometer at high radiation scenarios is mainly due to highly charged ions such as OVI [30] in the plasmas studied; they populate around the LCFS associated to helium-like OVII ions, which distribute broadly in the outer confined plasma region having a long life time. These charge states are less affected by the impurity sources. Clarifying to what extent the error field, drifts and the impurity sources correlate with the impurity radiation in the magnetic island chain is subject to future work. The correlation between the thermal and particle load of the target, as measured by IR cameras [68, 69], H_α-cameras, and divertor Langmuir probe arrays [70], and the impurity radiation in the SOL region, where the connection length is short, is therefore attractive to investigate because it may provide further clues for exploring the role of divertor impurity sources.

6. Summary

The bolometer tomography on W7-X, using an algorithm with a novel regularization functional based on relative gradient smoothing (RGS) of the sought emission profile, is validated using phantoms generated with EMC3-EIRENE modeling under real plasma conditions. The prior physical knowledge and boundary conditions incorporated in the RGS algorithm, such as numerical grids built on the magnetic flux surfaces and anisotropic smoothing in radial and poloidal directions, are essential to obtain reasonable tomographic reconstructions. Their reliability in dealing with asymmetric patterns is additionally evaluated.

Applying the algorithm to the bolometer measurements for W7-X plasma (during OP1.2a before wall boronisation) yields a clear picture of low-Z impurity radiation: (I) Radiation is predominantly located in the outer plasma region ($r/a > 0.8$) with individual intensity variations in poloidal and radial directions. (II) With increasing plasma density up to high radiation scenarios (approaching plasma detachment), the radiation zone shifts toward certain X-points, accompanied by a pronounced up-down asymmetry. The former feature is qualitatively consistent with theoretical expectations based on EMC3-EIRENE simulations (but no drifts included), while the up-down asymmetry is not. (III) The radiation asymmetry reverses when the direction of the toroidal magnetic field is reversed.

Further analysis of the poloidal variation of the radiation in the outer confined plasma region yields a magnitude of ~0.3 for r/a =0.9-0.95 in the high radiation scenarios for both magnetic field directions. This magnitude becomes smaller in lower density, lower radiation scenarios. This result suggests that the impurities and/or plasma parameters are unevenly distributed on the flux surfaces. Assuming that T_e and n_e are constant on the flux surface, this would imply that the impurity density shows variations of up to 30% in the outer confined plasma region, which is supported by SXR camera measurements. Based on the neoclassical theory of parallel transport, the ion-impurity collision frequency (determining the i-z frictional force) will have impacts on the impurity distribution. The observed radiation/impurity asymmetry is considered to be driven by the pronounced ion-impurity friction force at the plasma edge where the collisionality of the W7-X plasma is sufficiently high to meet the conditions for the development of neoclassical impurity asymmetries. The poloidal position on the flux surface where the impurity preferentially accumulates is likely to be associated with the magnetic field structure/direction, but we have also observed asymmetry reversal during experiments where the plasma volume became smaller (see the marks in Figure 3). This implies that other parameters, such as gradients and the radial electric field also affect the impurity distribution in W7-X.

Furthermore, numerical simulations using EUTERPE [19] and SFINCS [20, 71] are currently being performed to quantitatively explain the impurity distributions in the outer confined plasma region under real plasma conditions: The former assumes impurities in the tracer limit, while the latter requires the impurity density profile provided by 1D impurity transport simulations, since no diagnostic data are available. Preliminary results with both approaches show an asymmetry of the electrostatic potential on the flux surface, and the asymmetry changes sign after reversing the magnetic field direction. However, the absolute magnitude of the impurity asymmetry obtained is much smaller than the experimentally observed result (by a factor of ~10). In addition to the models themselves, the reasons for this could also be related to the boundary plasma parameters and their gradients used, which are subject to larger uncertainties. Further analyses are underway. Theoretical modeling to quantitatively explain the experimental results in the SOL remains a challenge.

ACKNOWLEDGEMEMT

One of the authors thanks Prof. P. Helander for his valuable discussions and general advice on the theoretical considerations, Dr. H. Meister and Mr. S. Schmitt (Fraunhofer IMM) for the cooperation in developing the bolometer detector, and Dr. M. Bernert for support in DAQ. This work was supported by the U.S. Department of Energy (DoE) under Grant DE-AC02-09CH11466, and DE-SC0014210. This work has been carried out within the framework of the EUROfusion Consortium and has received funding from the Euratom research and training programme 2014-2018 and 2019-2020 under grant agreement No 633053. The views and opinions expressed herein do not necessarily reflect those of the European Commission.

Reference

[1] Terry, J., et al., *Observation of Poloidal Asymmetry in Impurity-Ion Emission Due to* ∇B *Drifts.* Physical Review Letters, 1977. **39**(25): p. 1615.

[2] Brau, K., S. Suckewer, and S. Wong, *Vertical poloidal asymmetries of low-Z element radiation in the PDX tokamak.* Nuclear fusion, 1983. **23**(12): p. 1657.

[3] Smeulders, P., *Tomography of quasi-static deformations of constant-emission surfaces of high-beta plasmas in ASDEX.* Nuclear fusion, 1986. **26**(3): p. 267.

[4] Ingesson, L., et al., *Comparison of basis functions in soft x-ray tomography and observation of poloidal asymmetries in impurity density.* Plasma Physics and Controlled Fusion, 2000. **42**(2): p. 161.

[5] Burrell, K. and S. Wong, *Theoretical explanation of the poloidal asymmetry of impurity spectral line emission in collisional tokamak plasmas.* Nuclear Fusion, 1979. **19**(12): p. 1571.

[6] Chang, C.-S. and R. Hazeltine, *Impurity transport in the collisional regime for large poloidal variations.* Nuclear Fusion, 1980. **20**(11): p. 1397.

[7] Helander, P., *Bifurcated neoclassical particle transport.* Physics of Plasmas, 1998. **5**(11): p. 3999-4004.

[8] Reinke, M., et al., *Parallel transport studies of high-Z impurities in the core of Alcator C-Mod plasmas.* Physics of Plasmas, 2013. **20**(5): p. 056109.

[9] Fülöp, T. and P. Helander, *Nonlinear neoclassical transport in toroidal edge plasmas.* Physics of Plasmas, 2001. **8**(7): p. 3305-3313.

[10] Chechkin, V., et al., *Plasma flow asymmetries in the natural helical divertor of an l= 3 torsatron and their relation to particle losses.* Nuclear fusion, 2002. **42**(2): p. 192.

[11] Grigull, P., et al., *First island divertor experiments on the W7-AS stellarator.* Plasma physics and controlled fusion, 2001. **43**(12A): p. A175.

[12] Wenzel, U., et al., *Experimental observation of MARFEs in the W7-AS stellerator.* Plasma Physics and Controlled Fusion, 2002. **44**(10): p. L57.

[13] Peterson, B., et al., *Multifaceted asymmetric radiation from the edge-like asymmetric radiative collapse of density limited plasmas in the Large Helical Device.* Physics of Plasmas, 2001. **8**(9): p. 3861-3864.

[14] Thomsen, H., et al., *Radiative condensation and detachment in Wendelstein 7-AS stellarator.* Nuclear fusion, 2004. **44**(8): p. 820.

[15] Alonso, J., et al., *Parallel impurity dynamics in the TJ-II stellarator.* Plasma Physics and Controlled Fusion, 2016. **58**(7): p. 074009.

[16] Giannone, L., et al., *Bolometer tomography at the density limit of the HDH mode in the W7-AS stellarator.* Plasma physics and controlled fusion, 2003. **45**(9): p. 1713.

[17] Burhenn, R., et al., *On impurity handling in high performance stellarator/heliotron plasmas.* Nuclear Fusion, 2009. **49**(6): p. 065005.

[18] García-Regaña, J., et al., *On neoclassical impurity transport in stellarator geometry.* Plasma Physics and Controlled Fusion, 2013. **55**(7): p. 074008.

[19] García-Regaña, J., et al., *Electrostatic potential variation on the flux surface and its impact on impurity transport.* Nuclear Fusion, 2017. **57**(5): p. 056004.

[20] Mollén, A., et al., *Flux-surface variations of the electrostatic potential in stellarators: impact on the radial electric field and neoclassical impurity transport.* Plasma Physics and Controlled Fusion, 2018. **60**(8): p. 084001.

[21] Calvo, I., et al., *Electrostatic potential variations on stellarator magnetic surfaces in low collisionality regimes.* Journal of Plasma Physics, 2018. **84**(4).

[22] Calvo, I., et al., *Stellarator impurity flux driven by electric fields tangent to magnetic surfaces.* Nuclear Fusion, 2018. **58**(12): p. 124005.

[23] Velasco, J., et al., *Large tangential electric fields in plasmas close to temperature screening.* Plasma Physics and Controlled Fusion, 2018. **60**(7): p. 074004.

[24] Fujita, K., et al., *Study on impurity hole plasmas by global neoclassical simulation.* arXiv preprint arXiv:2104.12995, 2021.

[25] Bosch, H.-S., et al., *Technical challenges in the construction of the steady-state stellarator Wendelstein 7-X.* Nuclear Fusion, 2013. **53**(12): p. 126001.

[26] Beidler, C., et al., *Physics and engineering design for Wendelstein VII-X.* Fusion Technology, 1990. **17**(1): p. 148-168.

[27] Geiger, J., et al., *Physics in the magnetic configuration space of W7-X.* Plasma Physics and Controlled Fusion, 2014. **57**(1): p. 014004.

[28] Feng, Y., et al., *Comparison between stellarator and tokamak divertor transport.* Plasma physics and controlled fusion, 2011. **53**(2): p. 024009.

[29] Feng, Y., et al., *On the W7-X divertor performance under detached conditions.* Nuclear Fusion, 2016. **56**(12): p. 126011.

[30] Zhang, D., et al., *First observation of a stable highly dissipative divertor plasma regime on the Wendelstein 7-X stellarator.* Physical review letters, 2019. **123**(2): p. 025002.

[31] Schmitz, O., et al., *Stable heat and particle flux detachment with efficient particle exhaust in the island divertor of Wendelstein 7-X.* Nuclear Fusion, 2020. **61**(1): p. 016026.

[32] Zhang, D., et al., *Design criteria of the bolometer diagnostic for steady-state operation of the W7-X stellarator.* Review of Scientific Instruments, 2010. **81**(10): p. 10E134.

[33] Zhang, D., et al. *Optimization of Lines of Sight for Tomographic Reconstruction of the Bolometer Diagnostic at the W7-X Stellarator*. in *40th EPS Conference on Plasma Physics*. 2013. Citeseer.

[34] Anton, M., et al., *X-ray tomography on the TCV tokamak.* Plasma physics and controlled fusion, 1996. **38**(11): p. 1849.

[35] Fuchs, J., et al. *Twodimensional reconstruction of the radiation power density in ASDEX Upgrade*. in *21st EPS Conference on Controlled Fusion and Plasma Physics*. 1994. European Physical Society.

[36] Erckmann, V., et al., *Electron cyclotron heating for W7-X: Physics and technology.* Fusion science and technology, 2007. **52**(2): p. 291-312.

[37] Mast, K.F., et al., *A low noise highly integrated bolometer array for absolute measurement of VUV and soft x radiation.* Review of scientific instruments, 1991. **62**(3): p. 744-750.

[38] Meister, H., et al., *Broad-band efficiency calibration of ITER bolometer prototypes using Pt absorbers on SiN membranes.* Review of Scientific Instruments, 2013. **84**(12): p. 123501.

[39] Zhang, D., et al., *Determination of electron thermal diffusivity at the WEGA stellarator.* Nuclear Fusion, 2012. **52**(4): p. 043002.

[40] Meister, H., et al., *Bolometer developments in diagnostics for magnetic confinement fusion.* Journal of Instrumentation, 2019. **14**(10): p. C10004.

[41] Zhang, D., et al. *Thermal drift study on the bolometer diagnostic for steady-state fusion plasmas*. in *Proceedings of the 39th EPS Conference*. 2012.

[42] Giannone, L., K. Mast, and M. Schubert, *Derivation of bolometer equations relevant to operation in fusion experiments.* Review of Scientific Instruments, 2002. **73**(9): p. 3205-3214.

[43] Hirsch, M., et al. *The impact of microwave stray radiation to in-vessel diagnostic components*. in *AIP Conference Proceedings*. 2014. American Institute of Physics.

[44] Brandt, C., et al., *Soft x-ray tomography measurements in the Wendelstein 7-X stellarator.* Plasma Physics and Controlled Fusion, 2020. **62**(3): p. 035010.

[45] Mlynář, J., *Pixels method computer tomography in polar coordinates.* Czechoslovak Journal of Physics, 1995. **45**(10): p. 799-816.

[46] Williamson, J. and D. Evans, *Computerized tomography for sparse-data plasma physics experiments.* IEEE Transactions on Plasma Science, 1982. **10**(2): p. 82-93.

[47] Giannone, L., et al., *Tomography by the maximum entropy method for the W7-AS and W7-X multichannel bolometer systems.* Review of scientific instruments, 1997. **68**(1): p. 762-765.

[48] Li, D., et al., *Application of Bayesian tomography method to the visible spectroscopic diagnostic on HL-2A tokamak.* Plasma Physics and Controlled Fusion, 2021. **63**(3): p. 035002.

[49] Ingesson, L., et al., *Chapter 7: Tomography diagnostics: Bolometry and soft-x-ray detection.* Fusion Science and Technology, 2008. **53**(2): p. 528-576.

[50] Feng, Y., et al., *Physics of island divertors as highlighted by the example of W7-AS.* Nuclear fusion, 2006. **46**(8): p. 807.

[51] Effenberg, F., et al., *Numerical investigation of plasma edge transport and limiter heat fluxes in Wendelstein 7-X startup plasmas with EMC3-EIRENE.* Nuclear Fusion, 2017. **57**(3): p. 036021.

[52] Brunner, K., et al., *Real-time dispersion interferometry for density feedback in fusion devices.* Journal of Instrumentation, 2018. **13**(09): p. P09002.

[53] Pasch, E., et al., *The Thomson scattering system at Wendelstein 7-X.* Review of Scientific Instruments, 2016. **87**(11): p. 11E729.

[54] Pavone, A., et al., *Measurements of visible bremsstrahlung and automatic Bayesian inference of the effective plasma charge Zeff at W7-X.* Journal of Instrumentation, 2019. **14**(10): p. C10003.

[55] Zhang, D., et al., *Plasma radiation behavior approaching high radiation scenarios at W7-X*, submitted to Nuclear Fusion (2021).

[56] Summers, H. and R. McWhirter, *Radiative power loss from laboratory and astrophysical plasmas. I. Power loss from plasmas in steady-state ionisation balance.* Journal of Physics B: Atomic and Molecular Physics, 1979. **12**(14): p. 2387.

[57] Breton, C., C. De Michelis, and M. Mattioli, *Ionization equilibrium and radiative cooling of a high temperature plasma.* Journal of Quantitative Spectroscopy and Radiative Transfer, 1978. **19**(3): p. 367-379.

[58] Hsu, C.-T. and D. Sigmar, *Transport induced by ion-impurity friction in strongly rotating, collisional tokamak plasma.* Plasma physics and controlled fusion, 1990. **32**(7): p. 499.

[59] Braun, S. and P. Helander, *Pfirsch–Schlüter impurity transport in stellarators.* Physics of Plasmas, 2010. **17**(7): p. 072514.

[60] Braun, S. and P. Helander. *Pfirsch–Schlüter impurity transport in stellarator edge plasmas with large radial gradients*. in *Journal of Physics: Conference Series*. 2010. IOP Publishing.

[61] Beidler, C., et al., *Benchmarking of the mono-energetic transport coefficients—results from the International Collaboration on Neoclassical Transport in Stellarators (ICNTS).* Nuclear Fusion, 2011. **51**(7): p. 076001.

[62] Geiger, B., et al., *Observation of anomalous impurity transport during low-density experiments in W7-X with laser blow-off injections of iron.* Nuclear Fusion, 2019. **59**(4): p. 046009.

[63] Langenberg, A., et al., *Charge-state independent anomalous transport for a wide range of different impurity species observed at Wendelstein 7-X.* Physics of Plasmas, 2020. **27**(5): p. 052510.

[64] Wegner, T., et al., *Impact of the temperature ratio on turbulent impurity transport in Wendelstein 7-X.* Nuclear Fusion, 2020. **60**(12): p. 124004.

[65] Bozhenkov, S., et al., *Measurements and correction of the 1/1 error field in Wendelstein 7-X.* Nuclear Fusion, 2018. **59**(2): p. 026004.

[66] Lazerson, S.A., et al., *Error fields in the Wendelstein 7-X stellarator.* Plasma Physics and Controlled Fusion, 2018. **60**(12): p. 124002.

[67] Hammond, K., et al., *Drift effects on W7-X divertor heat and particle fluxes.* Plasma Physics and Controlled Fusion, 2019. **61**(12): p. 125001.

[68] Jakubowski, M., et al., *Infrared imaging systems for wall protection in the W7-X stellarator.* Review of Scientific Instruments, 2018. **89**(10): p. 10E116.

[69] Gao, Y., et al., *Methods for quantitative study of divertor heat loads on W7-X.* Nuclear Fusion, 2019. **59**(6): p. 066007.

[70] Rudischhauser, L., et al., *The Langmuir probe system in the Wendelstein 7-X test divertor.* Review of Scientific Instruments, 2020. **91**(6): p. 063505.

[71] Landreman, M., et al., *Comparison of particle trajectories and collision operators for collisional transport in nonaxisymmetric plasmas.* Physics of Plasmas, 2014. **21**(4): p. 042503.

Appendix. A comparison of the performance between the RGS- and MFR-method for bolometer tomography

As described in Section 3, we found that the RGS-method, based on relative gradient smoothing of the sought emission profile, is more suitable for W7-X bolometer tomography than the MFR-method, which is based on minimum Fischer information [34]. Here is an example for illustration. The phantom is created by adding a peak emission profile at the plasma center to a 2D profile with emission localized at the plasma boundary, which is the same as shown in Figure 5(a). The core part has an adjustable emissivity peak that allows testing the performance of tomography for the cases with pronounced radiation from the plasma center, possibly due to impurity accumulation or high-Z element; in this example, the maximum emissivity is $\varepsilon(0)$ = 0.1 W/cm^3 and the profile width is 10 cm. The phantom is shown in Figure 13.

Based on this phantom and the known geometric factors, the artificial signals for the HBC and VBC cameras are calculated based on Eq.(3). Gaussian noise with a relative level of 3% is added to the simulated signals. They are shown in Figure 13 (a) and (b), respectively. In addition, the channels with relatively high signals are indicated by their numbers (in the detector array of HBC, VBCl, and VBCr); the corresponding lines of sight (the dashed lines) are drawn on the phantoms for clarity.

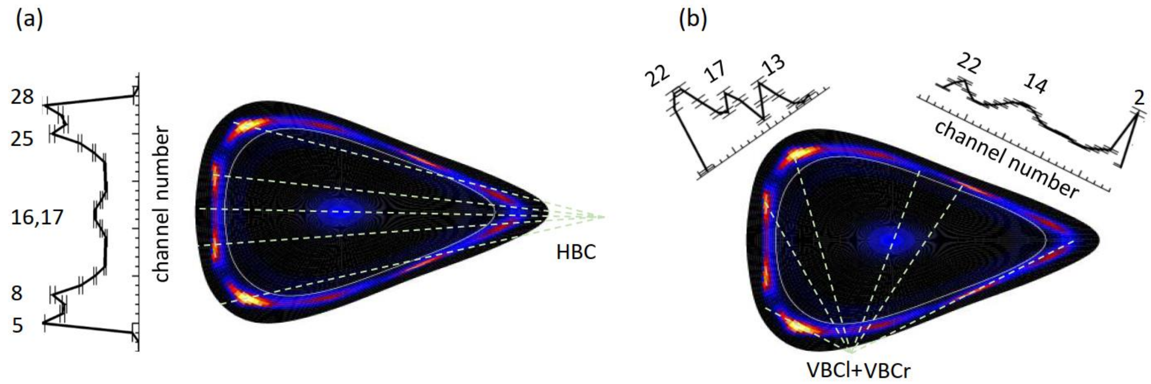

Figure 13 The 2D emissivity patterns created by adding a centrally peaked emissivity profile to the 2D profiles as shown in Figure 5(a) based on which artificial bolometer signals are forward calculated. Those for the HBC and VBC (both VBCl and VBCr) are shown in (a) and (b), respectively. Channels viewing intensive radiation volumes are marked by their numbers in the

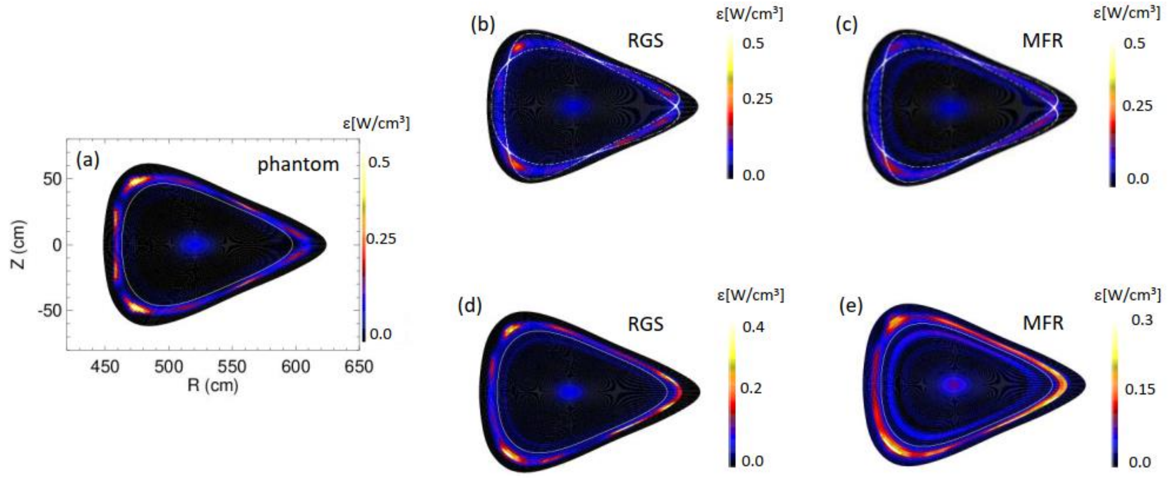

Figure 14. (a) The phantom created by adding oxygen impurity radiation pattern simulated by EMC3-Eirene code to a centrally peaked emission profile, based on which artificial bolometer signals are calculated; the reconstructed 2D radiation patterns using the synthetic bolometer signals based on the RGS and MFR algorithms are shown in (b) and (c), using the same color scale as in (a) for the phantom. Those in (d) and (e) are normalized to the maximum in (b) and (c), respectively, to show the 2D radiation pattern more clearly. The RGS-results have a greater similarity to the phantom while the MFR-results show visible artifacts like the clearly elevated emissions in the ring-shaped zone inside the separatrix. These results demonstrate that the RGS-method can better reconstruct the radiation pattern predicted by 3D modeling.

Using the same procedures as described in Section 3.2, the tomographic reconstructions were performed using the RGS- and MFR-algorithms. The results obtained are shown together with the phantom (for a better comparison) in Figure 14. The reconstruction from the MFR-method exhibits artifacts, such as the increased emissivity in the emission zone within the LCFS (in white). In contrast, the reconstruction obtained by the RGS-method can reproduce the radiation pattern in the phantom with higher similarity and more clearly resolve the detailed emission structures at the edge predicted by the modeling.

The up-down symmetric radiation feature from the 3D modeling phantoms is preserved within an uncertainty corresponding to the assumed Gaussian noise in the signals as well as numerical errors. It should be noted that χ^2~1 is normally achieved using both the RGS- and MFR-algorithms. These are routinely checked by comparing the forward and backward calculated bolometer signals based on the phantom and the tomogram, respectively (see Figure 6).

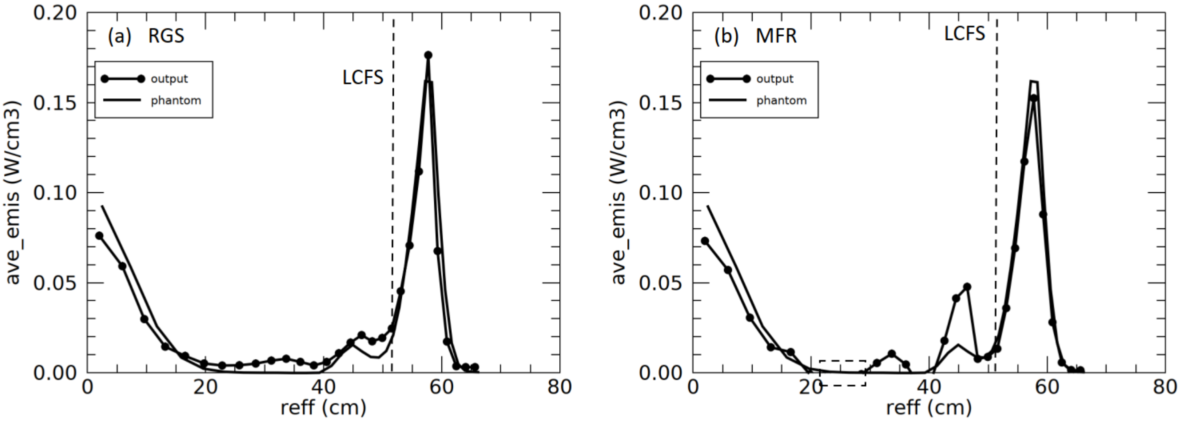

Figure 15. Comparisons of the radial profiles of the poloidally averaged emissivity based on the tomograms shown in Figure 14 obtained by RGS- and MFR-algorithms. They demonstrate the higher performance of the RGS-method by producing more accurate local emissivity in the tomogram. Marked rectangle in (b) encloses a region of negative emissivity (not shown).

The advantage of the RGS-method can be further illustrated by a comparison between the radial emission profiles obtained by poloidal averaging of the reconstruction and the phantom, which is shown in Figure 15 (a). That for the MFR-method is shown in Figure 15 (b). It can be seen that the profiles around the plasma center for both methods almost match the input profile (with an uncertainty of 10-15%). The disadvantages of the MFR-method can be seen in Figure 15 (b), where negative emissivity occurs at the radial positions enclosed by the dashed rectangle, and over-shooting occurs at *r* ~34 cm and 45 cm. In contrast, the RGS-method yields a clearly smaller difference, presenting a more reliable reconstruction. Moreover, this method shows a faster convergence in finding the solutions.